Heliyon 10 (2024) e33632

Contents lists available at ScienceDirect

Heliyon

journal homepage: www.cell.com/heliyon

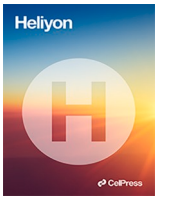

Research article

The role of thermal treatment and formulation on modifying the structural nature and optimizing certain physical features of coprecipitated superparamagnetic Co–Mn–Cr spinel ferrite

A.M. Elbashir [a], M.M. Seada [a,b], T.M. Meaz [b], E.H. El-Ghazzawy [b,*]

[a] Department of Physics, College of Science and Humanities, Prince Sattam Bin Abdulaziz University, Al-Kharj, 16273, Saudi Arabia
[b] Physics Department, Faculty of Science, Tanta University, Tanta, 31527, Egypt

ARTICLE INFO

Keywords:
Nano-ferrites
Structural and magnetic properties
Elastic parameters
Energy band gap
Dielectric properties

ABSTRACT

Examining the composition and heat treatment effects of co-precipitated $Co_{0.7}Mn_{0.3}Cr_xFe_{2-x}O_4$ (x = 0.0, 0.2, 0.4, 0.6, 0.8, and 1) ferrite nanoparticles provides valuable insights into the structural, morphological, optical, magnetic, and electrical properties of these materials. X-ray diffraction (XRD) and Rietveld refinement analyses confirm the spinel cubic crystalline phase of the samples, indicating the formation of well-defined crystal structures. Transmission electron microscope micrographs manifest the nanoscale nature of the produced specimens and their narrow particle size distribution with a small standard deviation. This uniformity is often desirable in many applications because it confirms the similarity of the properties and behaviors of the nanoparticles. The Fourier transform infrared spectroscopy study suggests that the substitution of Cr^{3+} ions at octahedral sites influences molecular stability. Annealing causes a slight expansion in bond length and a subsequent decrease in stability. The presence of Cr^{3+} ions enhances the strength of the specimens, while annealing weakens them. This indicates a fine balance between composition and processing conditions in determining the strength of the materials. The estimated optical indirect bandgap undergoes a redshift by adding Cr^{3+} ions. Annealing at elevated temperatures reduces the bandgap due to the quantum confinement effect, indicating the tunability of optical properties through compositional and thermal control. Samples with $x \geq 0.6$ exhibit nearly zero coercivity, indicating superparamagnetic behavior, which have promising applications. The preference of Cr^{3+} ions to occupy octahedral B-sites influences the magnetic behavior of the materials. The dielectric polarization and dielectric loss improved by adding Cr^{3+} ions, while the alternating current conductivity decreased. From impedance spectroscopy, the real and imaginary parts, Z' and Z", were increased by increasing Cr content. Furthermore, the annealing process greatly affects the electrical properties of the specimens. Overall, the study emphasizes the intricate relationship between composition, annealing conditions, and the resulting structural, magnetic, and electrical properties of Co–Mn–Cr ferrite nanoparticles, providing significant observations for the development of tailored materials for diverse applications in electronics, magnetics, and medicine.

* Corresponding author.
E-mail addresses: enas7777777@gmail.com, enas.elghazawi@science.tanta.edu.eg (E.H. El-Ghazzawy).

https://doi.org/10.1016/j.heliyon.2024.e33632
Received 3 March 2024; Received in revised form 16 June 2024; Accepted 25 June 2024
Available online 28 June 2024

1. Introduction

Due to their remarkable qualities, ferrimagnetic nanoparticles have received a lot of curiosity in contemporary research. These fields include data storage devices, biomedicine, magnetic resonance imaging, multi-chip inductor environmental cleanup, transformers, inductors, and catalysis [1,2]. Ferrites possess extraordinary magnetic properties in the nanoscale range, including super magnetism and spin behavior, including those of magnets with rapid spindles. Their surfaces can also tilt in different directions, exhibiting significant electrical resistance, permeability, and saturation magnetization [3]. Moreover, ferrite nanoparticles have a range of exciting technological uses in color imaging, magnetic refrigerators, high-frequency devices, and ferrofluids because they exhibit peculiar chemical, magnetic, electrical, mechanical, and structural characteristics [4]. Ferrites can be used in high-frequency applications because they have limited dielectric losses and eddy currents [3]. Changing the divalent or trivalent cation type (Cu^{2+}, Mg^{2+}, Co^{2+}, Ni^{2+}, Mn^{2+}, Zn^{2+}, Al^{3+}, and Cr^{3+}) controls the physical characteristics. The arrangement of cations throughout different lattice positions influences the main A-B super-exchange interaction among the metal ions. This in turn affects different magnetic properties of spinel ferrites, such as magnetization and anisotropy [5].

The mechanical strength and electrical conductivity of the obtained ferrite at the nanoscale differ substantially from those at the bulk size. There are also significant variations in the electronic structure. Each magnetic nanoparticle has a large surface area and quantum-size effects that show quantum tunneling of magnetization and superparamagnetic behavior. This exhibits a diversity in some magnetic properties [6].

It is important to mention here that ferrites containing manganese ions, such as Mn-ferrite, for example, are soft magnetic semiconducting materials. They also have low dielectric losses and high resistivity [5]. $MnFe_2O_4$ has strong saturation magnetization, strong cubic anisotropy, low core losses, and excellent chemical stability. On the other hand, the magnetically hard cobalt ferrite has an inverse spinel structure with a significant magnetostrictive coefficient, low eddy current losses, high coercivity, and cubic magnetocrystalline anisotropy. Mixed transition metals Mn–Co ferrites have superior magnetic and dielectric properties compared to Mn- or Co-ferrites, making them ideal for magneto-optical, magneto-mechanical, non-contact torque sensing, embedded stress sensing, and high magnetostriction applications [7]. These materials have widespread applications in various fields, such as recording devices, transducers, switching devices, and energy storage devices such as supercapacitors and batteries due of the significant magneto-mechanical effect and great sensitivity to stress [8–11].

Chromium-substituted ferrites have many applications in high-frequency devices, catalytic activity, and sensors because of their low hysteresis losses [1]. The electrical and magnetic characteristics of ferrite are significantly altered by the entry of chromium ions into the crystal lattice. Conductivity and dielectric constant decrease when chromium replaces iron [12]. The converse may occur, though, if it were added at the expense of a divalent ion, as this would raise the conductivity value, dielectric constant, and coercive field while lowering magnetization [13].

In addition, the researchers can apply the relationship between magnetic characteristics and cation distribution to control the material's magnetic behavior. Generally, the chromium ion prefers octahedral locations when substitution occurs in any spinel ferrite.

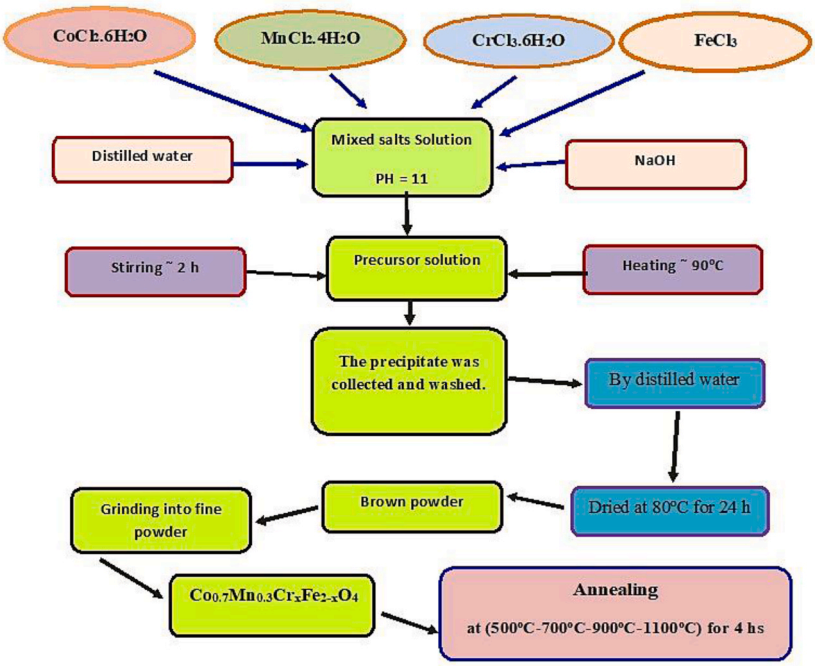

Fig. 1. Schematic diagram for the synthesis of the coprecipitated Co0.7Mn0.3CrxFex-2O4 nanoparticles.

Therefore, doping with chromium would result in a decrease in the degree of inversion (δ) and an alteration in the net magnetic moment. In other words, this enables the customization of magnetic properties to meet the needs of various technological applications [14].

Various methods, including sol-gel, hydrothermal, facile solvothermal, ball milling, and co-precipitation processes [15], can produce mixed spinel ferrite nanoparticles. Among these different methods, the authors prefer to use the co-precipitation method to obtain nanoparticles with the desired properties. High-yield fine-grained nanoparticles are coprecipitated in a short reaction time [11,16]. During synthesis, to avoid particle aggregations, surfactants like sodium dodecyl sulfate and oleic acid can be added to the solution [7,17]. The coprecipitation technique is based on reducing a mixture of metallic ions (e.g., Fe^{2+} and Fe^{3+}) using NaOH or NH_3OH as alkaline solutions. The high product purity, ease of reproducibility, nontoxicity, low cost, and absence of the necessity of using organic solvents are the main advantages of the coprecipitation process. However, the reaction factors (temperature, pH, ionic strength, kind of basic solution, and so forth) have a significant impact on the size, shape, and composition of the produced particles [18].

According to the functionality of ferrite nanoparticles, the authors always strive to develop and improve their properties to obtain the desired results in various promising applications. Therefore, this present work aimed to investigate the formation, structural and morphological characteristics, magnetic, optical, and electrical properties of mixed $Co_{0.7}Mn_{0.3}Cr_xFe_{2-x}O_4$ synthesized via the coprecipitation method followed by thermal treatment. The formation of crystalline phases, crystallite size, and lattice constant were studied by X-ray diffraction (XRD) and refined by Rietveld analysis. The specific surface area was determined by Brunauer-Emmett-Teller (BET) analysis. The shape, size, and size distribution of the particles and agglomeration were elucidated by transmission electron microscopy (TEM). The bond structure was monitored by Fourier transform infrared (FT-IR) spectroscopy. The magnetic properties were studied by a vibrating sample magnetometer (VSM). The optical properties and characteristics of the bandgap were examined by a UV–visible spectroscopy study. Finally, the dielectric properties, ac conductivity, and impedance spectroscopy were evaluated at room temperature using an LCR meter bridge.

2. Experimental

2.1. Sample preparation

The co-precipitation method [19] was used to prepare $Co_{0.7}Mn_{0.3}Cr_xFe_{2-x}O_4$ (x = 0.0, 0.2, 0.4, 0.6, 0.8, and 1), as shown in Fig. 1. NaOH solution was added dropwise to a mixed solution containing $CoCl_2.6H_2O$, $MnCl_2.4H_2O$, $CrCl_3.6H_2O$, and $FeCl_3$ with stoichiometric ratios until the pH value reached about 11. The preparation was performed according to the following chemical formula:

$$(2\text{-}x)\ FeCl_3 + 0.7(CoCl_2.6H_2O) + 0.3(MnCl_2.4H_2O) + x(CrCl_3.6H_2O) + 8NaOH$$

$$Co_{0.7}M_{0.3}Cr_xFe_{2-x}\ O_4 + 8NaCl + H_2O$$

The following table (Table 1) shows the number of moles of each reagent used in the synthesis process.

This mixture was heated and maintained at 90 °C for 2 h under continuous stirring to precipitate ferrite nanoparticles. The precipitated powder was then collected and thoroughly washed by distilled water, dried at 80 °C for 24 h, and finally ground in agate mortar to obtain ultrafine powder. $Co_{0.7}Mn_{0.3}Cr_xFe_{2-x}O_4$ (x = 0.0, 0.2, 0.4, 0.6, 0.8, and 1) samples were annealed at 900 °C for 4 h to study the compositional effect on different physical properties. While a selected sample, $Co_{0.7}Mn_{0.3}Cr_xFe_{2-x}O_4$ (x = 0.8), was annealed at different temperatures (500 °C, 700 °C, 900 °C, and 1100 °C) for 4 h to study the effect of annealing.

2.2. Characterization and measurements

2.2.1. X-ray diffraction analysis

A GNR APD 2000 Pro X-ray diffractometer (Cu-Kα radiation with λ = 1.54 Å) was used to characterize the crystallographic structure of the crystalline nanoparticles by operating at 40 kV and 30 mA. The effect of composition was studied for the samples $Co_{0.7}Mn_{0.3}Cr_xFe_{x-2}O_4$ (x = 0.0, 0.2, 0.4, 0.6, 0.8, and 1) annealed at a constant temperature of 900 °C. While the effect of annealing temperature on the crystal structure was studied for $Co_{0.7}Mn_{0.3}Cr_xFe_{x-2}O_4$ (x = 0.8) annealed at 500 °C, 700 °C, 900 °C and 1100 °C.

Table 1
Number of moles of each reagent used in the synthesis process

Sample	$FeCl_3$ No. of moles	$CoCl_2.6H_2O$ No. of moles	$MnCl_2.4H_2O$ No. of moles	$CrCl_3.6H_2O$ No. of moles	NaOH No. of moles
$Co_{0.7}Mn_{0.3}Fe_2O_4$	2	0.7	0.3	0	8
$Co_{0.7}Mn_{0.3}Cr_{0.2}Fe_{1.8}O_4$	1.8	0.7	0.3	0.2	8
$Co_{0.7}Mn_{0.3}Cr_{0.4}Fe_{1.6}O_4$	1.6	0.7	0.3	0.4	8
$Co_{0.7}Mn_{0.3}Cr_{0.6}Fe_{1.4}O_4$	1.4	0.7	0.3	0.6	8
$Co_{0.7}Mn_{0.3}Cr_{0.8}Fe_{1.2}O_4$	1.2	0.7	0.3	0.8	8
$Co_{0.7}Mn_{0.3}CrFeO_4$	1	0.7	0.3	1	8

2.2.2. Transmission electron microscopy (TEM)

The morphology, average particle size, and particle size distribution of the samples were studied by transmission electron microscopy (TEM) (JEOL JEM-2100). $Co_{0.7}Mn_{0.3}Cr_xFe_{x-2}O_4$ nanoparticles were sonicated after dispersing in an ethyl alcohol solution to separate the aggregations of the particles. Then a small amount of the sonicated solution was coated on a conductive copper-supported carbon grid. The grid was dried for a few minutes and then inserted into the TEM instrument under vacuum. A transmitted beam of electrons passed through the sample, and the scattered electrons were then detected to form a two-dimensional image at a high voltage of 80 kV [20].

2.2.3. Specific surface area (S_{BET})

The specific surface area of the nanoparticles was measured by the Brunauer-Emmett-Teller (BET) Micrometrics Instrument Corporation TriStar II 3020 V1.03. The material surface adsorbs gas molecules under different pressures to obtain the specific surface area.

2.2.4. Fourier transform infrared spectroscopy (FTIR)

To study the vibration modes of the chemical bonds, a Fourier transform infrared spectroscope (FT-IR) Bruker Tensor 27 was used in the range of 200–4000 cm^{-1} on KBr pellets containing the synthesized sample. This has been carried out to study the effect of composition and annealing temperature on $Co_{0.7}Mn_{0.3}Cr_xFe_{x-2}O_4$. An FT-IR spectroscopy study gives information about the molecular structure of materials, which can help in understanding the mechanical behavior of the materials. Additionally, the elastic constants

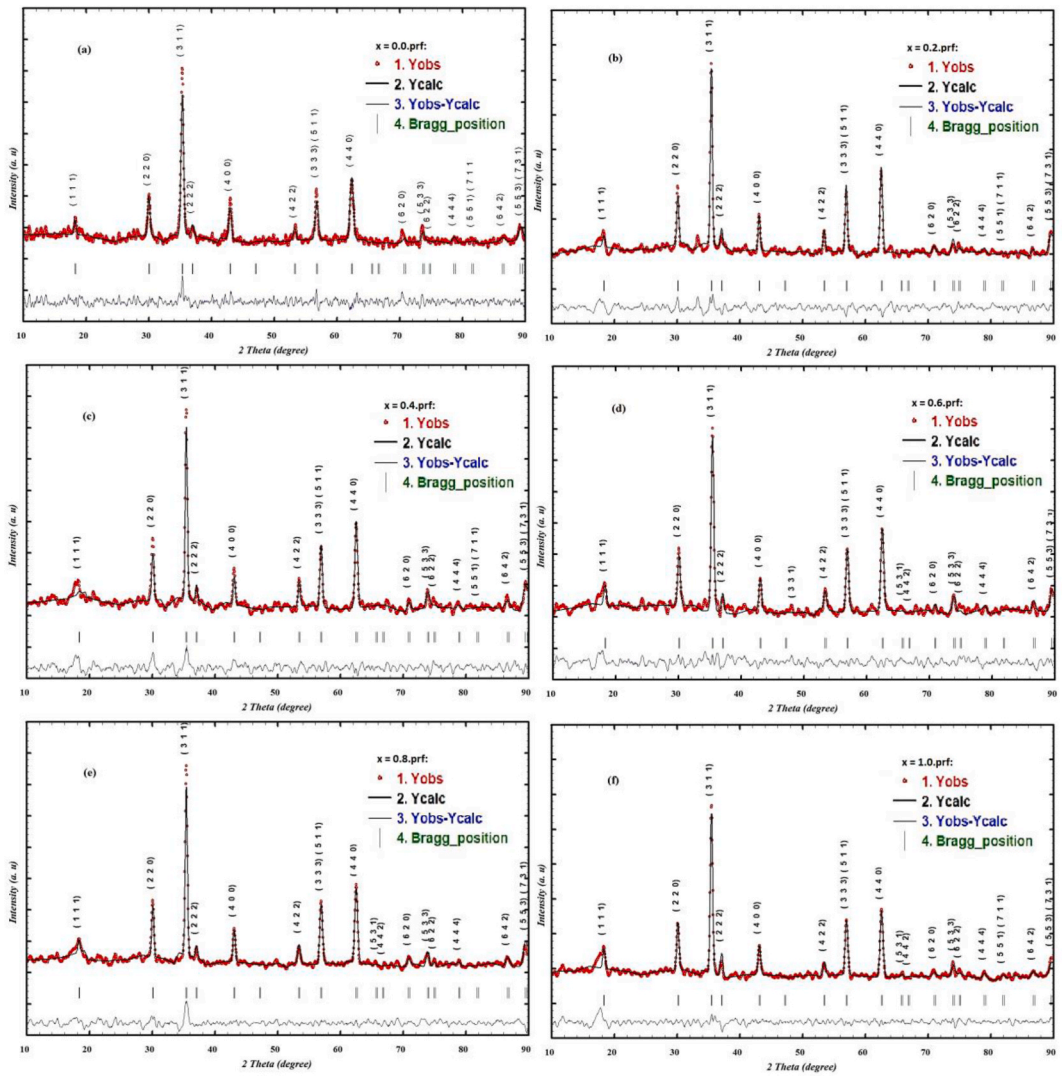

Fig. 2. Rietveld Refined XRD patterns of Co0.7Mn0.3CrxFex-2O4 annealed at 900 °C (a) x = 0.0 (b) x = 0.2 (c) x = 0.4 (d) x = 0.6 (e) x = 0.8 (f) x = 1.0.

and elastic moduli were determined using the FT-IR technique.

2.2.5. UV-VIS spectroscopy

A LAMBOMED, INC. double beam spectrophotometer recorded the optical absorption spectra in the visible and ultraviolet regions within the wavelength range of 200–1100 nm. Powders of different samples were dispersed in paraffin oil with a constant concentration, placed in a quartz cuvette of 10 mm path length (d), and subjected to ultraviolet and visible radiation to study their absorption spectra.

2.2.6. Vibrating sample magnetometer (VSM)

To study the magnetic properties of the samples and determine the magnetic parameters, a lab-built vibrating sample magnetometer can be used, and the experiment was carried out at room temperature up to a maximum field of 8 kOe. The vibrating sample was subjected to a magnetic field at a frequency of 40 Hz to be magnetized. Pickup coils piled on the electromagnet's poles experience a voltage due to the sample's vibration modulating the magnetic field lines. The frequency of the vibrating sample and the induced voltage are the same. The output signal from the pickup coils could be monitored from a lock-in amplifier. The induced magnetization is expressed by this signal (M). The value of H and the resulting M were recorded by the system to draw the M − H hysteresis loop.

2.2.7. The dielectric properties

AC electrical properties were investigated to study the effect of the composition of $Co_{0.7}Mn_{0.3}Cr_xFe_{x-2}O_4$ samples on their dielectric parameters. The measurements were performed at room temperature as functions of frequency in the range (100 Hz - 8 MHz) using an LCR meter (LCR METER IM3536-Hioki). The set up of the experiment includes pressing the powder samples under pressure of 3×10^8 N/m^2 into disc-shaped pellets with a diameter of 13 mm and a known thickness. The two circular surfaces of each pellet were coated with silver paste to make electrical contact with the two copper electrodes of an evacuated silica tube. This silica tube is designed to be connected to the LCR meter.

3. Results and discussion

3.1. X-ray diffraction analysis

The crystal structure analyses of $Co_{0.7}Mn_{0.3}Cr_xFe_{x-2}O_4$ (x = 0.0, 0.2, 0.4, 0.6, 0.8, and 1) annealed at 900 °C and $Co_{0.7}Mn_{0.3}Cr_{0.8}Fe_{1.2}O_4$ annealed from 500 °C to 1100 °C by step 200 °C were performed by refining the XRD results with the Rietveld analyses using the FULLPROF software program. The Y_{obs}-Y_{calc} curve represents the difference between the measured (observed Y_{obs}) and calculated (Y_{calc}) x-ray pattern, where it varies steadily as a function of 2θ, ensuring refinement stability. Fig. 2a-f displays the X-ray diffraction patterns of $Co_{0.7}Mn_{0.3}Cr_xFe_{x-2}O_4$ (x = 0.0, 0.2, 0.4, 0.6, 0.8, and 1) annealed at 900 °C and their refined curves. Table 2 lists the low values of χ^2 (an indicator of the goodness of fit), confirming the quality of the refinement. As compared to JCPDS Card No. 22–1086, the specimens have a single-phase cubic spinel structure with a space group of Fd-3m. The planes (111), (220), (311), (400), (422), (511), and (440) were easy to appear. Table 2 shows that the lattice constant, *a*, obtained from Rietveld analysis, slightly decreased once the chromium ions entered the crystal lattice. This change is attributed to the differences in ionic radii between Cr^{3+} (0.62 Å) and Fe^{3+} (0.67 Å) [21]. A little shrinkage of the unit cell occurs because of the accommodation of smaller ions at octahedral sites. Increasing Cr^{3+} content was found to decrease the x-ray theoretical density, ρ_x, as established elsewhere [22].

Porosity, *P%*, can be calculated using the relations; $P(\%) = 1 - \frac{\rho_B}{\rho_x}$ [23], where ρ_B is the bulk density and given by: $\rho_B = \frac{m}{\pi r^2 t}$, *r* and *t* are the radius and thickness of the disc samples [24].

The loss in molecular weight of the $Co_{0.7}Mn_{0.3}Cr_xFe_{x-2}O_4$ molecule due to the relatively low atomic mass of chromium indeed can

Table 2
The goodness of fit, (χ^2), lattice constant, *a* (Å), crystallite size, R (nm), the lattice strain, ε, theoretical XRD density, ρ_x (g/cm^3), porosity %, and the hopping length (jump distance), $L_{A\text{-}A}$, $L_{B\text{-}B}$, and shared sites, $L_{A\text{-}B}$, calculated based on Rietveld analysis, and the specific surface area, S_{BET} (m^2/g), for $Co_{0.7}Mn_{0.3}Cr_xFe_{x-2}O_4$ (x = 0.0, 0.2, 0.4, 0.6, 0.8, and 1) annealed at 900 °C and $Co_{0.7}Mn_{0.3}Cr_xFe_{x-2}O_4$ (x = 0.8) annealed at 500 °C, 700 °C, 900 °C, and 1100 °C.

Sample	χ^2	(*a*) (A°)	R (nm)	$\varepsilon \times 10^{-3}$	ρ_x (g/cm^3)	Porosity (%)	$L_{A\text{-}A}$ (Å)	$L_{B\text{-}B}$ (Å)	$L_{A\text{-}B}$ (Å)	S_{BET} (m^2/g)
0.0	0.112	8.4240	22.73	5.325	5.1863	48.60	3.6477	2.9783	3.4924	50.90
0.2	0.159	8.4002	20.87	4.225	5.2134	51.87	3.6374	2.9699	3.4825	55.14
0.4	0.146	8.4036	19.24	3.675	5.1898	51.61	3.6389	2.9711	3.4839	60.09
0.6	0.155	8.4039	18.8	2.758	5.1720	51.78	3.6389	2.9712	3.4841	61.71
0.8	0.147	8.4041	17.79	1.425	5.1543	50.57	3.6390	2.9713	3.4842	65.43
1.0	0.13	8.3947	17.22	0.85	5.1544	50.74	3.6350	2.9679	3.4803	67.60
Effect of annealing temperature on $Co_{0.7}Mn_{0.3}Cr_{0.8}Fe_{1.2}O_4$										
T°C	χ^2	(*a*) (A°)	R (nm)	$\varepsilon \times 10^{-3}$	ρ_x (g/cm^3)	Porosity (%)	$L_{A\text{-}A}$ (Å)	$L_{B\text{-}B}$ (Å)	$L_{A\text{-}B}$ (Å)	S_{BET} (m^2/g)
500	0.132	8.3645	6.70	6.93	5.2279	46.88	3.6219	2.9573	3.4677	171.30
700	0.148	8.3832	12.06	3.15	5.1930	50.56	3.6300	2.9639	3.4755	95.81
900	0.146	8.4041	17.79	1.425	5.1543	50.58	3.6391	2.9713	3.4842	65.43
1100	0.148	8.4077	21.61	0.6	5.1477	51.24	3.6407	2.9726	3.4857	53.94

lead to an increase in porosity, as shown in Table 2.

The Williamson-Hall equation [25–27] was used to calculate the average crystallite size, R, and the induced lattice strain, ε, of $Co_{0.7}Mn_{0.3}Cr_xFe_{x\text{-}2}O_4$:

$$\beta_{hkl}\cos\theta = \frac{0.94\lambda}{R} + 4\varepsilon\sin\theta \tag{1}$$

where β_{hkl} is the peak broadening obtained from the Rietveld analysis. The average crystallite size exhibits a slight drop from 22.73 nm to 17.221 nm by substituting smaller ionic-radius Cr^{3+} ions [28]. Introducing smaller Cr^{3+} ions into spinel lattices indeed has a notable effect on the induced tensile strain within the material. This phenomenon aligns with variations in the lattice constant. The reduction in lattice constant, mentioned before, is associated with a decrease in induced tensile strain. This correlation between doping levels, lattice constant, and induced tensile strain is important for understanding the mechanical behavior of the material, as will be explained in the following discussion. The consistency in crystal size observed in this study, compared to other studies using the chemical coprecipitation method, is intriguing. It suggests that the synthesis method plays a significant role in determining the resulting crystal size within the material [29,30]. For example, the mean crystal size of the magnetite and NiMg ferrite samples is about 15.2 [31] nm and 11.6 nm [24], respectively. As a result, compared to other preparation techniques, the chemical precipitation process is characterized by the fact that the precipitated material has an extremely fine crystalline size. Moreover, the presence of ions like Cr^{3+} may influence the nucleation and growth processes during precipitation and reduce the size. Samples generated using different techniques do not exhibit this effect. $Ni_{0.6}Mg_{0.2}Co_{0.2}FeCrO_4$ and $Ni_{0.1}Co_{0.5}Cu_{0.4}Fe_{1.7}Cr_{0.3}O_4$, which were synthesized using the sol-gel process and annealed at 850 °C, had typical crystal sizes of 124 nm [32] and 103 nm [21], respectively.

Because of the high electron-lattice interaction, electrons in spinel ferrites are often localized rather than entirely free. The charge displacements produced by nearby ions trap these electrons in potential wells. A displacement zone with a radius significantly smaller than the unit-cell dimension is referred to as a tiny polaron [33]. The relation between the Cr substitution and the deformation of the spinel lattice influences the radius, jump distance, and jump activation energy of polarons [34].

The hopping length (jump distance) in the tetrahedral site (L_A), octahedral site (L_B), and shared sites ($L_{A\text{-}B}$) was calculated from equation (2) [35]:

$$L_{A-A} = a\frac{\sqrt{3}}{4}, L_{B-B} = a\frac{\sqrt{2}}{4} \text{ and } L_{A-B} = a\frac{\sqrt{11}}{8} \tag{2}$$

The variation of $L_{A\text{-}A}$, $L_{B\text{-}B}$, and shared sites $L_{A\text{-}B}$ reflects the same behavior as the lattice parameter. They usually go down along with increasing chromium content, as seen in Table 2. This is known as the shrinkage of the unit cell. The accommodation of smaller Cr^{3+} ions into the octahedral lattices causes a decrease in site radius, resulting in the shrinkage of the unit cell. So, the larger ions

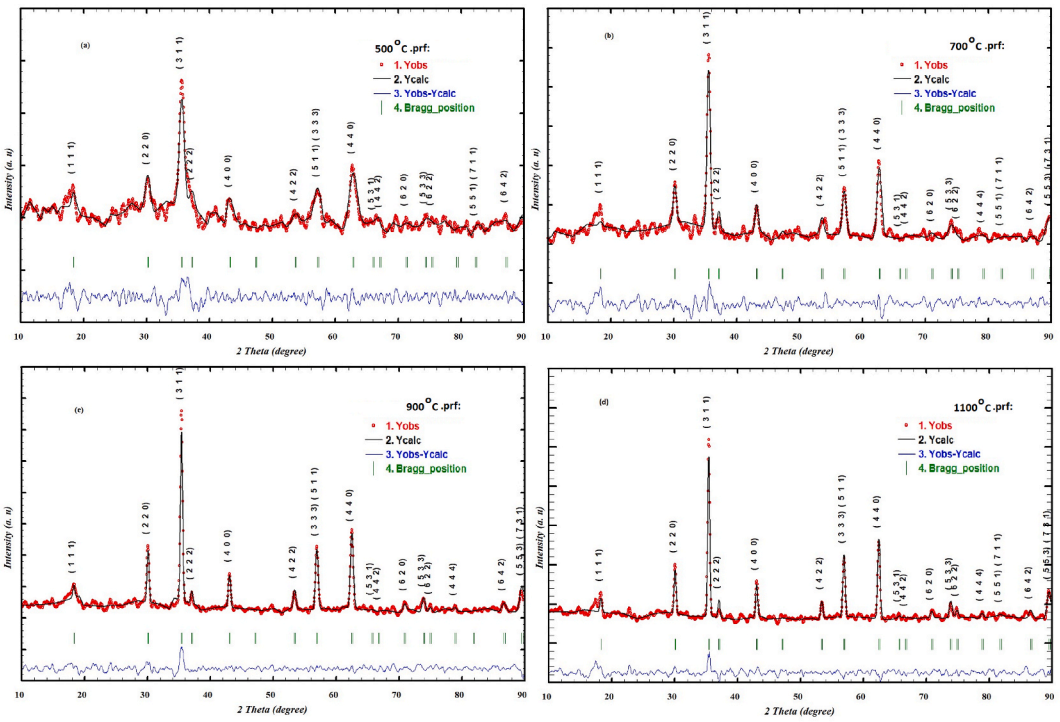

Fig. 3. Rietveld Refined XRD patterns of Co0.7Mn0.3CrxFex-2O4 (x = 0.8) annealed at: (a) 500 °C (b) 700 °C (c) 900 °C (d) 1100 °C.

occupy the tetrahedral lattices [36]. Therefore, understanding these structural variations is essential for optimizing the properties of spinel ferrite materials for various applications.

The annealing process at different temperatures (500 °C, 700 °C, 900 °C, and 1100 °C for 4 h) had a great effect on the sample $Co_{0.7}Mn_{0.3}Cr_xFe_{2-x}O_4$ (x = 0.8), as shown in Fig. 3a–d. This is shown by the stronger and wider XRD peaks. During the annealing process, the elevated temperature allows atoms to move more freely in the crystal, facilitating the rearrangement of atomic positions, and this leads to getting rid of the internal stresses. Consequently, the crystal becomes more perfect, and the grain boundary volume is diminished [37]. It is noticed that the sample annealed at 500 °C has relatively broad peaks, confirming its ultra-fine nature and small crystallite size.

The lattice constant, a, of $Co_{0.7}Mn_{0.3}Cr_xFe_{2-x}O_4$ (x = 0.8) and the hopping distances, $L_{A\text{-}A}$, $L_{B\text{-}B}$, and $L_{A\text{-}B}$, have gone up with annealing. Annealing can have various effects on the properties of materials, including crystal growth and changes in oxidation states of ions. Annealing can reduce Fe^{3+} ions to Fe^{2+} ions and stimulates crystal growth. The divalent cation Fe^{2+} (0.76 Å) has a larger ionic radius than the trivalent one, Fe^{3+} (0.64 Å), as known [21]. This increases the effective ionic radius and affects the packing of ions in the crystal lattice. The unit cell expansion, which is interpreted by increasing the unit cell volume ($v = a^3$), leads to an observed drop in the theoretical XRD density and a subsequent rise in porosity, as displayed in Table 2. The lattice strain, ε, has a continuous decrease with annealing. This suggests the enhancement of the crystallization process by further annealing.

Based on the refinement of the atomic occupancy values in Rietveld analysis, the cation distribution between tetrahedral and octahedral sites of $Co_{0.7}Mn_{0.3}Cr_xFe_{2-x}O_4$ annealed at 900 °C was determined and listed in Table 3. Throughout the Rietveld refinement process, the cation occupancies at tetrahedral and octahedral sites are confined to maintain the stoichiometry of the synthesized ferrites. It is important to note that the thermal treatment of the samples and the previous processing circumstances both highly affect the cation distribution. Most Mn^{2+} and Co^{2+} ions partially occupy the octahedral B-sites, which reveal that CoMn ferrite nanoparticles have a partially inversed spinel structure [20]. While the Fe^{3+} ions are distributed randomly over tetrahedral and octahedral sites. According to the findings, Fe^{3+} ions transferred from their octahedral sites to the tetrahedral ones by entering Cr^{3+} ions, which prefers octahedral sites.

The degree of inversion is defined as the proportion of Fe^{3+} in the A-site. It increases by adding chromium ions, and this behavior is consistent with the slight drop in lattice constant when iron is substituted by chromium ions [25].

Furthermore, there is a considerable dependence of the cation distribution on the two sublattices on the annealing temperature. Mn^{2+} and Cr^{3+} ions moved from the B-site to the A-site together with Fe^{3+} ions. While the distribution of Co^{2+} ions was not affected.

By comparing the crystal structure of the present samples with those of others published in the literature (see Table 4), it is typically focused on XRD parameters such as lattice constants, theoretical density, crystallite size, strain, and porosity. The lattice constant and theoretical density of different spinel ferrites may differ slightly because of the variation in synthesis conditions and electronic configuration [7]. While the crystal size and porosity values are different because of the different histories of heat treatment for each sample as well as the cation distribution. These various synthetic conditions can govern and control the properties of the obtained spinel ferrites [11]. These affect greatly the structural, magnetic, and electrical properties of these materials, which can be used in a variety of applications such as magnetic recording media, microwave devices, and magnetic sensors.

3.2. Transmission electron microscopy (TEM)

To get better insight into the morphology and size of the particles, TEM images were obtained on powders. Therefore, the morphology and shape of the grains can be clearly seen, as shown in Fig. 4a-d and Fig. 5a-d for the samples $Co_{0.7}Mn_{0.3}Cr_xFe_{2-x}O_4$ (x = 0, 0.2, 0.4, and 1) as-synthesized and annealed at 900 °C, respectively. From TEM images, the particles appear to take multiple forms, some of which have a nearly spherical shape, others have asymmetric agglomerations, and some have an elongated shape.

Embedding Cr^{3+} ions into the crystal lattice of ferrite evidently minimizes the size of the particles in the as-synthesized samples. On the other hand, there is an enormous variation in the particle size when comparing the particle sizes of the as-synthesized and the annealed $Co_{0.7}Mn_{0.3}Cr_xFe_{2-x}O_4$ nanoparticles. The as prepared and annealed samples have average particle sizes ranging from 3 nm to 26.3 nm and 15.88 nm–37 nm, respectively, as displayed in Table 5. The annealed nano ferrites have a relatively large number of

Table 3
The cation distribution of $Co_{0.7}Mn_{0.3}Cr_xFe_{x-2}O_4$ (x = 0.0, 0.2, 0.4, 0.6, 0.8, and 1) annealed at 900 °C and $Co_{0.7}Mn_{0.3}Cr_xFe_{x-2}O_4$ (x = 0.8) annealed at 500 °C, 700 °C, 900 °C, and 1100 °C.

Sample	A-site	B-site
0	$Co_{0.179}Mn_{0.091}Fe_{0.697}$	$Co_{0.521}Mn_{0.209}Fe_{1.303}$
0.2	$Co_{0.167}Mn_{0.085}Cr_{0.054}Fe_{0.783}$	$Co_{0.533}Mn_{0.\ 215}Cr_{0.146}Fe_{1.217}$
0.4	$Co_{0.179}Mn_{0.106}Cr_{0.119}Fe_{0.792}$	$Co_{0.521\ }Mn_{0.194}Cr_{0.281}Fe_{1.208}$
0.6	$Co_{0.183}Mn_{0.054}Cr_{0.157}Fe_{0.987}$	$Co_{0.517}Mn_{0.246}Cr_{0.443}Fe_{1.013}$
0.8	$Co_{0.179}Mn_{0.081}Cr_{0.215}Fe_{0.811}$	$Co_{0.521}Mn_{0.219}Cr_{0.585}Fe_{1.189}$
1	$Co_{0.179}Mn_{0.074}Cr_{0.126}Fe_{0.932}$	$Co_{0.521}Mn_{0.226}Cr_{0.874}Fe_{1.068}$
Effect of annealing temperature on $Co_{0.7}Mn_{0.3}Cr_{0.8}Fe_{1.2}O_4$		
T (^{O}C)	A-site	B-site
500	$Co_{0.184}Mn_{0.096}Cr_{0.217}Fe_{0.614}$	$Co_{0.516}Mn_{0.204}Cr_{0.583}Fe_{1.386}$
700	$Co_{0.186}Mn_{0.112}Cr_{0.221}Fe_{0.630}$	$Co_{0.514}Mn_{0.\ 188}Cr_{0.580}Fe_{1.370}$
900	$Co_{0.179}Mn_{0.081}Cr_{0.215}Fe_{0.811}$	$Co_{0.521}Mn_{0.219}Cr_{0.585}Fe_{1.189}$
1100	$Co_{0.182}Mn_{0.063}Cr_{0.209}Fe_{0.861}$	$Co_{0.518\ }Mn_{0.237\ }Cr_{0.591\ }Fe_{1.139}$

Table 4
Comparative table of different XRD parameters: lattice constant *a* (Å), crystallite size R (nm), theoretical XRD density ρ_x (g/cm^3), porosity % for different spinel ferrites.

Sample	(*a*) (A^o)	ρ_x (g/cm^3)	R (nm)	Porosity %	Ref.
$Mn_{0.9}Zn_{0.3}Si_{0.2}Fe_{1.6}O_4$	8.497	4.94	29.47	14	[38]
$Ni_{0.6}Mn_{0.4}Fe_2O_4$	8.354	5.039	25.94	–	[39]
$Li_{0.35}Co_{0.3}FeO_4$	8.394	4.48	53	24.57	[40]
$Ni_{0.4}Mg_{0.6}Fe_2O_4$	8.360	4.869	23.81	–	[39]
$Ai_{0.1}Ti_{0.2}Zn_{0.3}Ni_{0.4}Fe_2O_4$	8.359	5.630	19	19	[34]
$MgCr_{0.5}Fe_{1.5}O_4$	8.376	5.12	58.54	–	[14]
$Ni_{0.7}Cu_{0.3}Al_{0.06}Fe_{1.54}O_4$	8.337	5.195	55.63	26.23	[41]

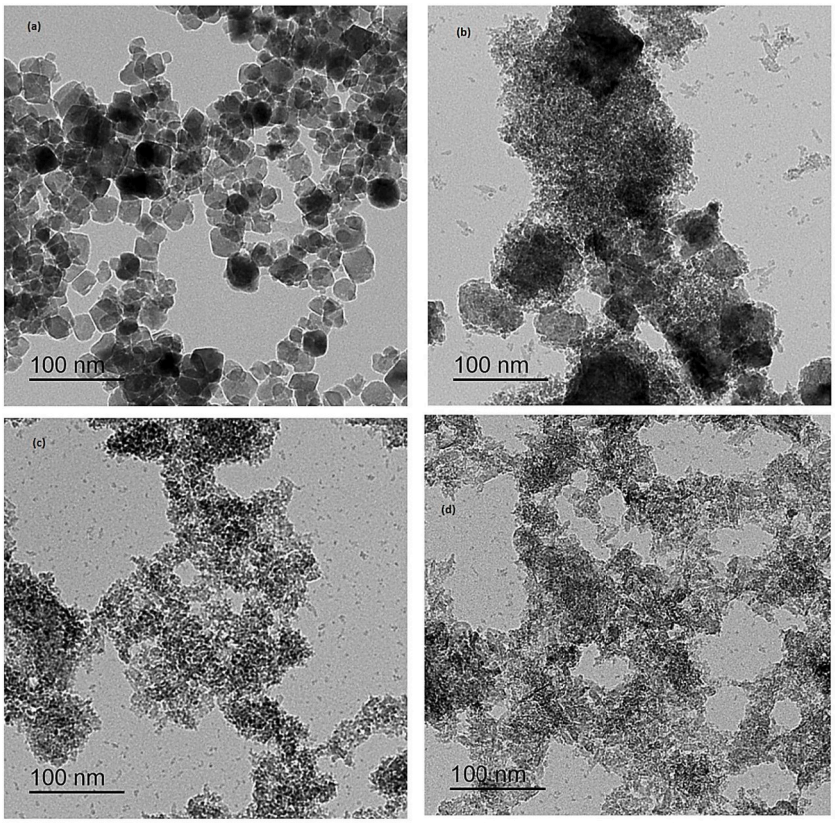

Fig. 4. a)TEM images of the as-synthesized Co0.7Mn0.3CrxFex-2O4 (a) x = 0.0 (b) x = 0.2 (c) x = 0.4 (d) x = 1.0. (b)Particle size distribution (theoretically fitted using Gaussian distribution function) of the as-synthesized Co0.7Mn0.3CrxFex-2O4 (a) x = 0.0 (b) x = 0.2 (c) x = 0.4 (d) x = 1.0.

clusters of nanograins. Two essential factors contribute to this: (i) the exchange interaction produced by the magnetic dipole moment of the magnetic lattice; (ii) the elevating annealing temperature of the synthesized nano-ferrite (900 °C), resulting in the interaction among nano-grains [42].

Compared to the findings provided in the XRD studies, the average grain size is noticeably larger than the crystallite size. While XRD only offers information on the crystalline regions of the grains and not the amorphous parts. TEM examination, on the other hand, supplies knowledge on the overall shape of the grains as a whole. Taking a closer look at the literature, the coprecipitated $MnCoFe_2O_4$ sample has a grain size ranging from 30 to 40 nm [43]. While TEM images of $Ni_{0.7}Zn_{0.3}Fe_2O_4$, $Ni_{0.4}Zn_{0.3}Mn_{0.3}Fe_2O_4$, $Ni_{0.4}Zn_{0.3}$-$Co_{0.3}Fe_2O_4$, and $Ni_{0.4}Zn_{0.3}Cu_{0.3}Fe_2O_4$, which were prepared by the sol-gel method, exhibit different shapes and sizes, with average particle sizes of 41, 21, 32, and 40 nm, respectively [44]. The findings in this study agree with the literature, as seen.

The particle size distribution is analyzed and interpreted using TEM images and ImageJ software, and the histograms are shown in Fig. 4(a–d) and 5 (a-d). It is important to note that narrow particle size distributions suggest uniformity in particle size, which can be desirable for many applications. Additionally, the samples have small standard deviation values, as seen in Table 5. This means that the particles have sizes close to each other around the mean value.

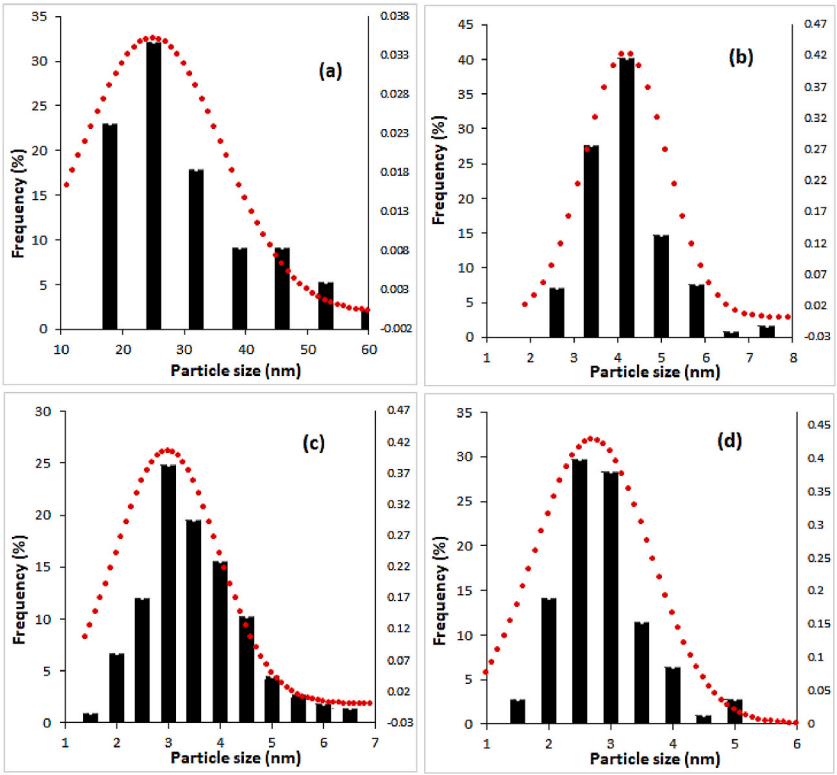

Fig. 4. (*continued*).

In the present work, although HRTEM provides information about the internal morphology of the nanocrystals, it typically provides limited information about the material's surface topography. Surface topography like morphology, surface roughness, and defects can be detected by other techniques such as scanning electron microscopy (SEM) and atomic force microscopy (AFM). For a deep examination of the material, a combination of HRTEM data and surface topography analysis (SEM and AFM) should be performed.

On the other hand, it is better to study and identify the properties of the nanoparticles by combining TEM and EDAX data. This combination helps to visualize the morphology, crystal structure, and elemental composition of the materials.

3.3. Specific surface area (S_{BET})

This measurement is critical to comprehending the physical properties and possible applications of the present nanoparticles. The relationship between S_{BET} and various factors, such as Cr^{3+} ion content and annealing temperature, can provide insight into nanoparticle reactivity and performance. Table 2 displays that the specific surface area, S_{BET}, of the nanopartticles increases with an increase in Cr^{3+} ion content and decreases with annealing. This confirms the presence of an inverse relationship between a specific surface area and particle size. This, in turn, can control the surface reactivity of the nanoparticles.

3.4. Fourier transform infrared spectroscopy study (FT-IR)

By analyzing the characteristic absorption bands in FTIR spectra, the functional groups present in the nanoparticles and the ferrite phase can be identified, which helps in understanding their chemical structure and composition. The nature of the chemical bonds studied based on the vibrational frequency which depends on the cation mass, distance between cation and oxygen ion, and bonding force [45].

The FT-IR study covers the wavenumber range from 200 to 4000 cm^{-1}. Fig. 6a displays the FT-IR spectra of $Co_{0.7}Mn_{0.3}Cr_xFe_{2-x}O_4$ (x = 0.0, 0.2, 0.4, 0.6, 0.8, and 1) annealed at 900 °C. The obtained spectra have seven absorption bands: ν_1, ν_2, ν_3, ν_T, ν_{Th}, ν_A, and ν_B. The first band, ν_1, ranges from 580 to 599 cm^{-1}, and the second band, ν_2, ranges from 381 to 487 cm^{-1}. These values are similar to those published before [46,47]. They are intrinsic stretching lattice vibrations of the tetrahedral bonds and intrinsic bending vibrations of the octahedral bonds, respectively, of ferrites, as shown in Table 6 [48]. These two vibrational bands are the result of the metal-oxygen bond's intrinsic vibrations, which verify the production of spinel ferrite material and the completion of the reaction [49]. Since the vibrational frequency depends on the bonding force, length, and cation mass, the observed difference between ν_1 and ν_2 values is related to the shorter bond length of oxygen-metal ions at the tetrahedral sites [49]. ν_1 and ν_2 exhibit a slight shift toward higher frequencies by further adding Cr^{3+} ions; this is due to changing the Me–O^2-internuclear distance of the tetrahedral and

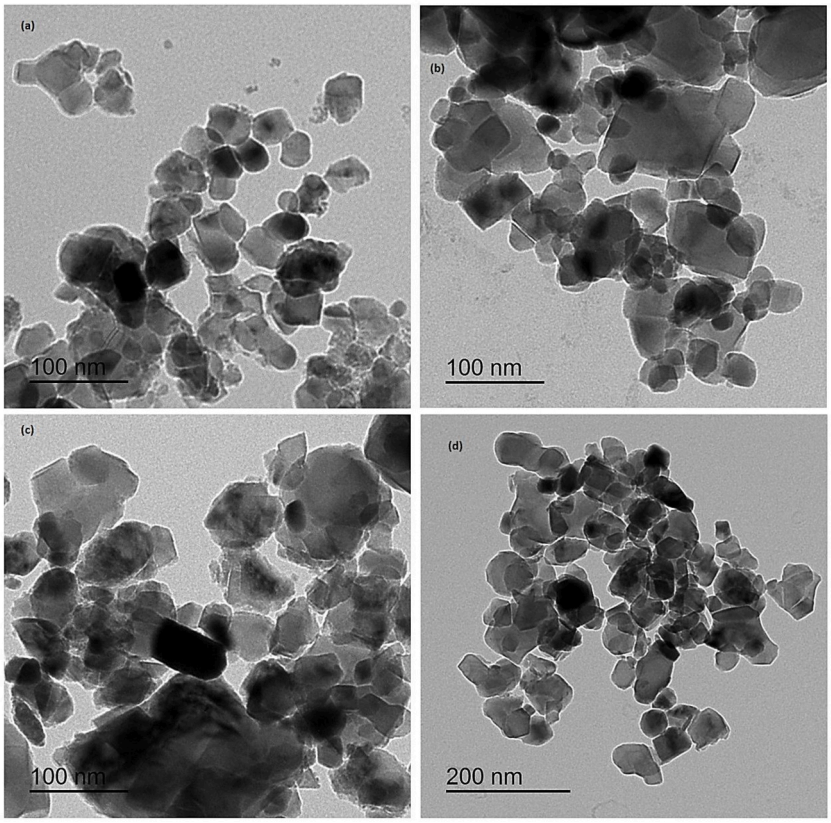

Fig. 5. (a)TEM images of Co0.7Mn0.3CrxFex-2O4 annealed at 900 °C (a) x = 0.0 (b) x = 0.2 (c) x = 0.4 (d) x = 1.0. (b)Particle size distribution (theoretically fitted using Gaussian distribution function) of the annealed Co0.7Mn0.3CrxFex-2O4 (a) x = 0.0 (b) x = 0.2 (c) x = 0.4 (d) x = 1.0.

octahedral sites. These observations are in agreement with previous publications [50].

Additionally, a weak band, ν_3, appears in the samples $Co_{0.7}Mn_{0.3}Cr_xFe_{2-x}O_4$ (x = 0.0, 0.2, 0.4) that may be due to the splitting ν_2 band because of divalent metal ion-oxygen bond formation at octahedral sites (Co^{2+} and Mn^{2+} ions in the present samples). According to the cation distribution, relatively high proportions of Fe^{3+} ions exist at octahedral sites in lower Cr content samples. Some of these Fe^{3+} ions may be reduced to Fe^{2+} by the annealing process at 900 °C. Furthermore, the band ν_A in the range 877 cm^{-1} to 873 cm^{-1} is usually related to the existence of divalent cations at A-sites. However, ν_B in the range 1047–1049 cm^{-1} may be associated with the presence of tetravalent metal ion-oxygen, Fe^{4+}-O^{2-} and/or Cr^{4+}-O^{2-}. Electron hopping between Cr^{3+} and Fe^{3+} ions may produce Fe^{4+} and/or Co^{4+} [50].

The hydroxyl group (OH) appears in the spectra as a triple band, ν_T, around 1539 cm^{-1} for all the samples.

A known restoring force should restore the relative displacement between nuclei during molecular vibration at certain frequencies. Therefore, the force constant (a measure of the stiffness of the chemical bond) is a second-order derivative of the potential energy. It is correlated to the bond length and hence the vibrational frequency by the relations [51]:

$$F_A = 4\pi^2 c^2 \nu_1^2 \mu, F_B = 4\pi^2 c^2 \nu_2^2 \mu \quad (3)$$

The force constant rises as the bond length shortens, as displayed in Table 7. The substitution of Cr^{3+} ions at the octahedral sites instead of Fe^{3+} ions may cause the bond lengths in the octahedral sites to contract slightly. This is the reason why F_A and F_B rise with composition (x). Additionally, the absorption bands around 3460 cm^{-1} correspond to water molecules with tensile bonds, and the hydroxyl intervals (O–H) exhibit variations accordingly [52].

On the other hand, Fig. 6b displays the FT-IR spectra of $Co_{0.7}Mn_{0.3}Cr_xFe_{2-x}O_4$ (x = 0.8) annealed at different temperatures. As known, the annealing process causes an expansion in the bond length that reduces ν_1 and ν_2 values. The shifting of ν_1 and ν_2 to lower frequencies clearly confirms the linearity of the relationship between the bond length and annealing temperatures.

Moreover, the triple band, ν_T, exists in all spectra and disappeared when the sample was annealed at 1100 °C. This is because annealing at elevated temperatures causes the material to get rid of residual moisture, which leads to the separation of the OH bonds from the ferrite molecule.

The force constants, F_A and F_B, have a slight decrease with annealing, as shown in Table 7, which may be ascribed to lengthening the interatomic separation that leads to weakening the Me–O^{2-} bonds at the A- and B-sites.

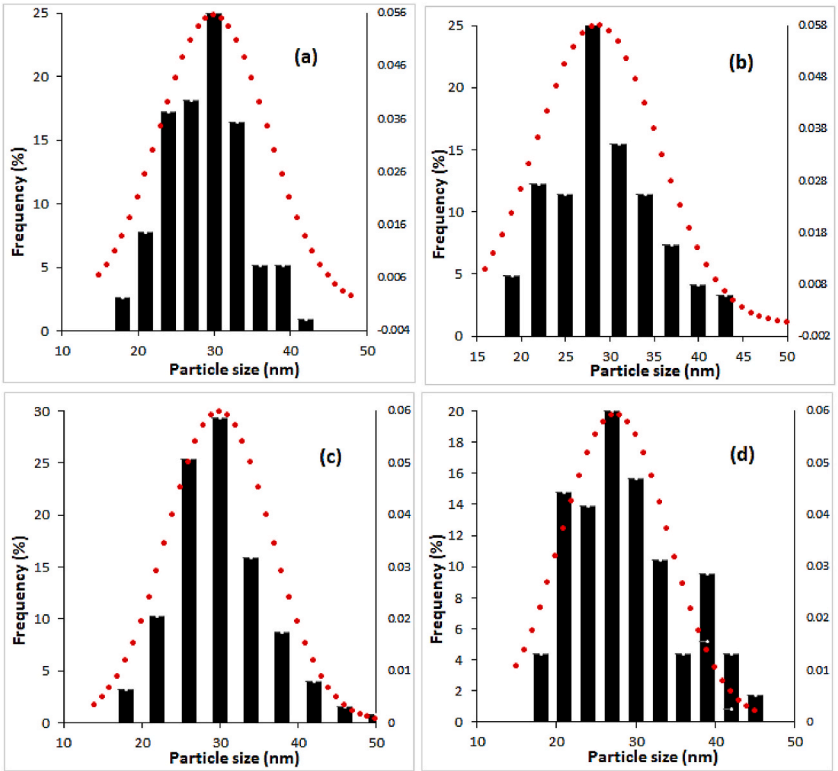

Fig. 5. (*continued*).

Table 5
Particle size (nm) of $Co_{0.7}Mn_{0.3}Cr_xFe_{x-2}O_4$ (x = 0.0, 0.2, 0.4, and 1), as synthesized and annealed at 900 °C from TEM.

Average particle size (nm)			Standard deviation	
Sample	As-synthesized	Annealed	As-synthesized	Annealed
0.0	26.3	29.85	11.33	7.20
0.2	4.3	27	0.942	6.88
0.4	3	30	0.982	6.67
1.0	2.5	26.5	0.930	6.73

It is worth mentioning that the temperature at which a crystal exhibits its maximum normal mode of vibration is known as the Debye temperature, Θ_D. The Debye temperature demonstrates the stability of the crystal lattice [53]. Below Θ_D, the electrons traverse through the lattice planes with limited scattering, and consequently, the atomic motion is constrained. While the electron scattering rises significantly above Θ_D. Therefore, the material becomes more stable when its Θ_D is high [54]. Debye temperature, Θ_D, was determined from: $\Theta_D = \frac{hc\upsilon_{AV}}{2\pi k}$ [54]. In the present samples, Θ_D increases with x from 690 to 780 k by increasing Cr^{3+} content, as illustrated in Table 7. This means that the crystal lattice becomes more stable when the interatomic bonding strength hardens [55].

On the other hand, since heating weakens the strength of the interatomic bonding, there is a noticeable decrease in Θ_D with increasing the annealing temperature, as shown in Table 7. This decrease is related to a slight reduction in vibrational frequencies.

3.4.1. Elastic properties

In light of the enormous practical importance of nano-crystalline ferrites in industrial and technological applications, the mechanical properties of these materials are significant. As a result of magnetostriction and piezomagnetic effects, stress generates alterations to magnetization. Abrupt shocks can also cause domain-wall motion [47]. This study postulates that the present samples are isotropic and that there is no crystallographic relation between the stress and the resulting deformation.

Elastic constants, or elastic moduli, are used to express the response of an isotropic, homogeneous solid to an applied force, and these elastic moduli are interrelated. It is known that stiffness is analogous to the modulus of elasticity. Therefore, the stiffness constants C_{11} and C_{12}, bulk modulus (B), Young's modulus (E), and rigidity (shear) modulus (G) were determined from the equations established before [56,57]. The stiffness constants and elastic moduli exhibit an increase with increasing Cr^{3+} ion content, as listed in Table 7. This may be related to the reduction in crystal size. This means that reducing the grain size enables the overall grain boundaries to grow excessively. These grain boundaries are helpful in hindering dislocation and dispersion through the crystal. This, in

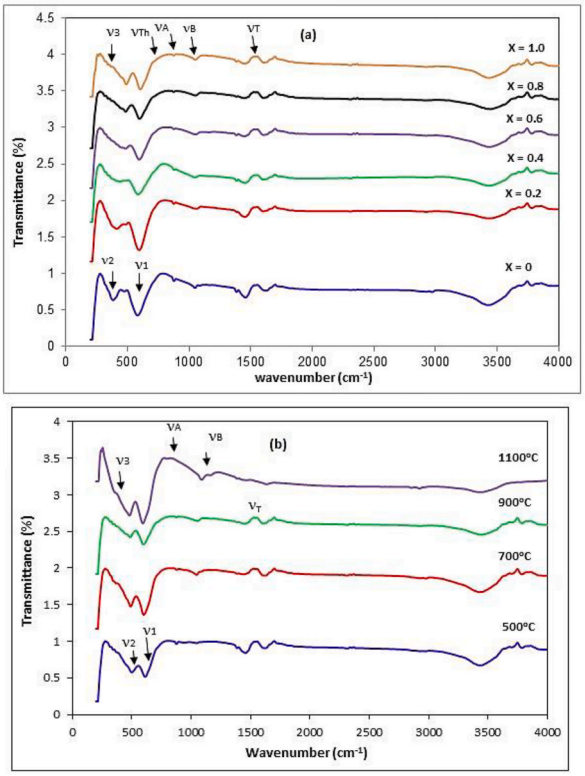

Fig. 6. FTIR spectra of: (a) Co0.7Mn0.3CrxFex-2O4 (x = 0.0, 0.2, 0.4, 0.6, 0.8, and 1) annealed at 900 °C (b) Co0.7Mn0.3CrxFex-2O4 (x = 0.8) annealed at 500 °C, 700 °C, 900 °C and 1100 °C.

Table 6
The vibrational frequencies in (cm^{-1}), ν_1, ν_2, ν_3, ν_A, ν_B, ν_T, and the energy band gap, E_g, **(eV)** of $Co_{0.7}Mn_{0.3}Cr_xFe_{x\text{-}2}O_4$ (x = 0.0, 0.2, 0.4, 0.6, 0.8, and 1) annealed at 900°C and $Co_{0.7}Mn_{0.3}Cr_xFe_{x\text{-}2}O_4$ (x = 0.8) annealed at 500 °C, 700 °C, 900 °C, and 1100 °C.

X	ν_1 (cm^{-1})	ν_2 (cm^{-1})	ν_3 (cm^{-1})	ν_A (cm^{-1})	ν_B (cm^{-1})	ν_T (cm^{-1})	E_g (eV)
0	580	381	314	877	1047	1535	0.899
0.2	594	410	314	873	1055	1539	0.842
0.4	584	437	316	877	1045	1539	0.815
0.6	595	445	314	877	1049	1539	0.61
0.8	595	484	316	875	1049	1541	0.558
1	599	487	316	873	1049	1541	0.523
Effect of annealing temperature on $Co_{0.7}Mn_{0.3}Cr_{0.8}Fe_{1.2}O_4$							
T(°C)	**ν_1 (cm^{-1})**	**ν_2 (cm^{-1})**	**ν_3 (cm^{-1})**	**ν_A (cm^{-1})**	**ν_B (cm^{-1})**	**ν_T (cm^{-1})**	E_g (eV)
500	609	498	316	876	1045	1573	0.992
700	599	489	316	878	1044	1566	0.673
900	595	484	316	875	1049	1541	0.558
1100	592	480	277	797	1086	–	0.534

turn, improves the strength and hardness of the material.

The effect of thermal annealing on the stiffness constants and elastic moduli was studied. On the contrary, the annealing process results in a slight drop in the elastic moduli and stiffness constants. It is crucial to consider that the annealing process forces grains to grow, which limits the number of grain boundaries that obstruct molecular transport [37]. This allows the formation of dislocations, and consequently, the crystal becomes comparatively weaker. It is worth noting that the values of stiffness constants and elastic moduli are in agreement with those in the literature [47].

3.5. Ultraviolet and visible spectroscopy

For optoelectronic applications, it is crucial to investigate room-temperature optical characteristics such as electromagnetic radiation absorption and transmission [58]. A variety of aspects, including surface roughness, oxygen deficiency, lattice constant, dopant concentration, and crystallite size, influence the optical characteristics of the nanoparticles [59].

Table 7
Stiffness constants, C_{11}, C_{12}, elastic moduli, B, Y, and G, force constants (N/m), F_A, F_B, and Debye temperature, θ_D of $Co_{0.7}Mn_{0.3}Cr_xFe_{x-2}O_4$ (x = 0.0, 0.2, 0.4, 0.6, 0.8, and 1) annealed at 900°C and $Co_{0.7}Mn_{0.3}Cr_xFe_{x-2}O_4$ (x = 0.8) annealed at 500 °C, 700 °C, 900 °C, and 1100 °C.

X	C11 (GPa)	C_{12} (GPa)	B (GPa)	Y (GPa)	G (GPa)	F_A (N/m)	F_B(N/m)	θ_D
0	211.47	402.0	97.29	198.62	115.17	246.09	106.19	691
0.2	228.33	398.7	102.69	216.47	124.32	258.12	122.97	722
0.4	232.41	408.7	104.71	220.18	126.55	249.49	139.70	734
0.6	242.48	424.5	109.13	229.82	132.03	258.96	144.86	748
0.8	256.83	464.2	116.55	242.61	139.87	258.99	171.37	776
1	261.37	470.3	118.47	247.024	142.34	262.48	173.50	781
Effect of annealing temperature on $Co_{0.7}Mn_{0.3}Cr_{0.8}Fe_{1.2}O_4$								
T (°C)	C11 (GPa)	C12 (GPa)	B (GPa)	Y (GPa)	G (GPa)	FA	F_B	θ_D
500°C	271.85	53.94	126.57	253.98	148.021	271.31	181.42	796
700°C	262.99	47.55	119.36	248.42	143.23	262.47	174.93	782
900°C	256.83	46.42	116.56	242.62	139.88	258.98	171.37	776
1100°C	253.20	44.98	114.38	239.63	137.89	256.38	168.55	771

Fig. 7a and b displays the UV–Vis optical absorption spectra (the absorbance *vs.* wavelength (200–1100 nm) plot) of $Co_{0.7}Mn_{0.3}Cr_xFe_{x-2}O_4$ (x = 0.0, 0.2, 0.4, 0.6, 0.8, and 1) annealed at 900 °C and $Co_{0.7}Mn_{0.3}Cr_xFe_{x-2}O_4$ (x = 0.8) annealed at different temperatures. All the samples manifest better absorbance in the visible region than in the UV region.

Tauc's relation produces the energy bandgap of the materials: $(\alpha h\upsilon) = A\,(E_g - h\nu)^n$. Where E_g is the material's bandgap energy and 'n' is a factor based on the semiconducting material's valence band to conduction band transition. For the indirect and direct bandgaps,

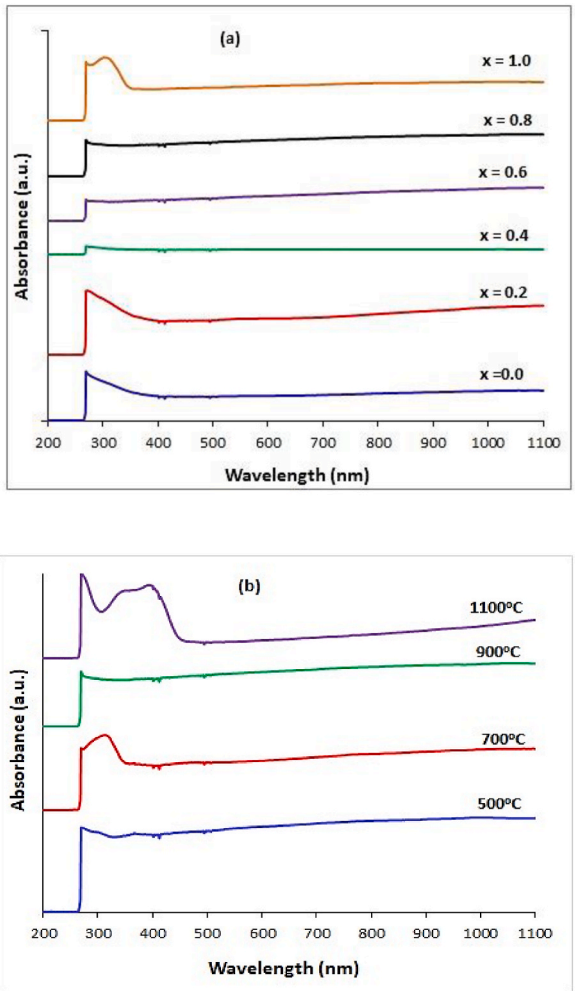

Fig. 7. UV–vis spectra of: (a) Co0.7Mn0.3CrxFex-2O4 (x = 0.0, 0.2, 0.4, 0.6, 0.8, and 1) annealed at 900 °C (b) Co0.7Mn0.3CrxFex-2O4 (x = 0.8) annealed at 500 °C, 700 °C, 900 °C and 1100 °C.

the value of n fluctuates between ½ and 2, respectively [60]. In the present investigation, the estimated indirect bandgap energy, where n = ½, is tabulated in Table 6. As the proportion of Cr^{3+} ions go up, the bandgap energy decreases. The generation of sub-bandgap energy levels within the bandgap, which may have been caused by interface defects and vacancies, can be accompanied by a little shrinkage of the bandgap [61].

On the other hand, by increasing the annealing temperature from 500 °C to 1100 °C, E_g decreases slightly, which is assigned to the quantum confinement phenomenon, as shown in Table 6. The decrease in E_g with a little crystallite size magnification demonstrates the quantum size effect [62]. As a result, even tiny variations in crystal size have a significant impact on the energy band gap. Consequently, the practically constant absorption edge (304 nm) is the result of the crystal size's restricted fluctuation range. Each studied sample requires nearly the same amount of absorbed photon energy for the electronic transition. Predominantly, reducing E_g could be the result of a drop in the band gap between the O-2p and Fe-3d levels [63]. E_g values of $Cu_{0.25}Co_{0.25}Mg_{0.5-x}Ni_xCe_{0.03}Fe_{1.97}$ are 0.87 eV [64], which is in agreement with the present data. However, E_g of $CoFe_2O_4$ and $MnFe_2O_4$ [59] are 3.86 eV and 4.02 eV, respectively, which are higher than the present data because of their tiny particle size (10 nm).

3.6. Magnetic measurements using VSM

To analyze and study the action of the Cr^{3+} ion and the thermal annealing process on the magnetic properties of a series of $Co_{0.7}Mn_{0.3}Cr_xFe_{x-2}O_4$ nano-crystalline compounds, VSM measurements were performed at room temperature. The chemical composition, the distribution of cations, the preparation technique, and the particle size all have an enormous impact on the magnetic properties [52]. The magnetic parameters as functions of composition (x) and annealing temperature were extracted from the hysteresis curves (Fig. 8a, b, c) and listed in Table 8. The magnetic parameters, saturation magnetization, and coercivity values are in good agreement with those of other spinel ferrite samples, $Ni_{0.5-x}Zn_xCo_{0.5}Fe_{2-y}Al_yO_4$ [65] and $CoR_{0.1}Fe_{1.9}O_4$ [66]. Adding different transition metals (Zn^{2+}, Cu^{2+}, Co^{2+}, Mn^{2+}, Ni^{2+}, etc.) to spinel ferrite can alter their magnetic properties. The functionality of the present samples can be improved by changing their magnetic moment. P. Monisha et al. [59] studied the effect of Mn^{+2} doping on $CoFe_2O_4$ nanoparticles prepared via the co-precipitation method. The magnetic interaction between the A and B sub-lattices is reduced as a result of the substitution of Mn^{2+} ions into sub-lattice B, lowering the value of M_s. In the case of pure $CoFe_2O_4$, the value of M_s is 34.20 emu/g, which is less than the bulk value (80 emu/g). A similar result was reported by other researchers [20]. On the other hand, the M_s and H_c values of $MgCr_xFe_{2-x}O_4$ [14] decrease by adding nonmagnetic Cr^{3+}, from 20.7 to 4.6 emu/g and 127 to 40 Oe, respectively.

The aforementioned samples have a soft superparamagnetic nature, as demonstrated by the S-shaped hysteresis loops. The superparamagnetic behavior of these samples is a result of the tiny sizes of the crystallites and their low magnetic anisotropy, which permit their easy thermal activation [67]. The present samples are single-domain magnetic particles that have nearly zero coercivity, low remanent magnetization, relatively high saturation magnetization, and a very low squareness ratio. These aspects make the samples have a superparamagnetic nature [67].

Additionally, their blocking temperature is located below room temperature, except for the low chromium content samples (x = 0.0, 0.2, 0.4) [68].

All the present samples reveal low saturation magnetization values, M_s. The core-shell model explains this phenomenon. Every magnetic particle possesses both a core and a shell, according to the core-shell model. The shell, often known as the dead layer or disordered domain boundary, lacks magnetic order, while the core possesses magnetic order (ordered domains). Therefore, the surface-to-volume ratio has a great effect when the particles possess a tiny size (the effect of the dead layers). The size effect of the nanoparticles leads to non-collinearity or canting of spins on their surface, consequently decreasing the magnetization [52]. Saturation magnetization and coercivity values are comparable with earlier investigated Co-based spinel ferrite nanoparticles [35,69]. However, samples in the present study have lower M_s than $Co_{1-x}Cr_xFe_2O_4$ [69] because of the presence of non-magnetic Mn^{2+} ions. This result is in good agreement with those reported in earlier publications [12].

It is expected that M_s decreases when substituting Cr^{3+} ions because it has a lower magnetic moment than Fe^{3+} ions. However, M_s changes according to the estimated cation distribution from the Rietveld analysis in Table 3. Néel's theory of ferrimagnetism and the arrangement of cations between different sites demonstrate the magnetic behavior of ferrites. The net magnetic moment, or theoretical magnetic moment, m_{th}, in the Bohr magneton unit (μ_B) is equal to the vector sum of the moments of the two sublattices ($m_{th} = M_B\text{-}M_A$),

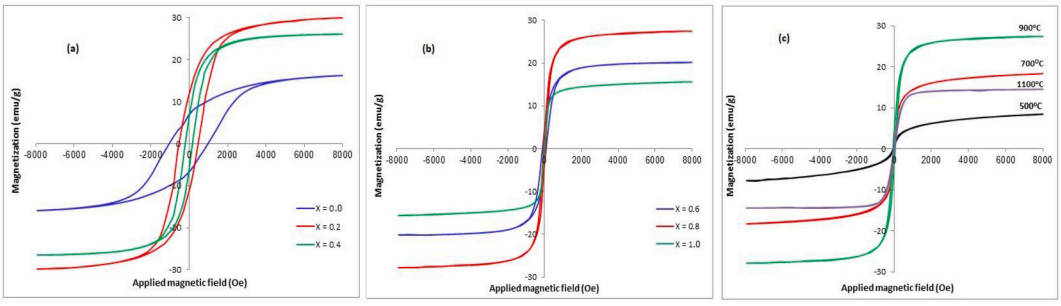

Fig. 8. Magnetization curves of Co0.7Mn0.3CrxFex-2O4 (a) x = 0.0, 0.2, 0.4, annealed at 900 °C (b) x = 0.6, 0.8, 1.0, annealed at 900 °C (c) Co0.7Mn0.3CrxFex-2O4 (x = 0.8) annealed at different temperature.

Table 8
The saturation magnetization M_s (emu/g), remnant magnetization M_r (emu/g), squareness ratio SQR (M_r/M_s), coercivity H_c, theoretical and experimental magnetic moments, m_{th} (μ_B), m_{exp} (μ_B), Yaffet-Kittel angle, (θ_{YK}), and the anisotropy constant, K_1 (erg/g), of $Co_{0.7}Mn_{0.3}Cr_xFe_{x-2}O_4$ (x = 0.0, 0.2, 0.4, 0.6, 0.8, and 1) annealed at 900°C and $Co_{0.7}Mn_{0.3}Cr_xFe_{x-2}O_4$ (x = 0.8) annealed at 500 °C, 700 °C, 900 °C, and 1100 °C.

X	M_s (emu/g)	M_r (emu/g)	M_r/M_s	H_c (Oe)	m_{th} (μ_B)	m_{exp} (μ_B)	θ_{YK}	K_1 (erg/g)
0	16.17	6.8	0.421	988	4.482	0.676	54.6	16641.63
0.2	29.92	11.57	0.387	471	4.878	1.246	51.8	14679.5
0.4	26.15	5.99	0.229	171	4.025	1.086	46.6	4657.969
0.6	20.19	3.92	0.194	89	2.424	0.835	34.8	1871.781
0.8	27.44	3.49	0.127	52	4.722	1.132	49.2	1486.333
1	15.55	0.547	0.035	11	4.713	0.639	51.8	178.1771
Effect of annealing temperature on $Co_{0.7}Mn_{0.3}Cr_{0.8}Fe_{1.2}O_4$								
T (°C)	M_s (emu/g)	M_r (emu/g)	M_r/M_s	H_c (Oe)	m_{th} (μ_B)	m_{exp} (μ_B)	θ_{YK}	K_1 (erg/g)
500°C	7.85	0.71	0.090	57	4.288	0.348	52.2	466.0938
700°C	18.43	1	0.054	54	4.588	0.760	50.9	1036.688
900°C	27.44	3.49	0.127	52	4.722	1.130	49.2	1486.333
1100°C	14.49	0.69	0.048	21	4.418	0.598	51.3	316.9688

which is based on the magnetic moment of each cation in the two sublattices. It is equal to 5μ_B for both Fe^{3+} and Mn^{2+} ions and 3μ_B for Co^{2+} and Cr^{3+} ions. Moreover, the m_{exp} which is presented in Tables 8 and is found using [32]:

$$m_{exp} = \frac{M_s\left(\frac{emu}{g}\right) \times MW\left(gmol^{-1}\right)}{\mu_B \times N_A\ mol^{-1} \times 10^3} \tag{4}$$

Where MW is the molecular weight of the sample, μ_B is Bohr magneton (=9.274×10-24 J/T), and N is Avogadro's number. The m_{exp} exhibits the same behavior as m_{th} (see Table 6), which confirms the accuracy of the cation distribution. The experimental values of the magnetic moment are lower than the theoretical ones because of the assumption of the presence of non-colinear spin order [70]. This can be explained based on the Yaffet and Kittel (Y–K) model.

By applying the formula: $m_{exp} = M_B \cos\theta_{YK} - M_A$, the spin Y–K angle ($\theta_{YK}$) was computed. A non-zero $\theta_{Y\text{-}K}$ reveals that the super-exchange interactions weaken. Additionally, the octahedral spins are no longer arranged completely antiparallel to the tetrahedral spins, which could lead to a drop in magnetization [71].

It is also noted that when the annealing temperature rises, the particle size increases, leading to a decrease in the disorder at the nanoparticle surface. This allows the spins to align with the field, which in turn increases magnetization. However, the sample annealed at 1100 °C has lower magnetization due to its cation distribution and the subsequent reduction in the magnetic moment.

Furthermore, increasing the concentration of Cr^{3+} reduces the coercivity, H_c, due to the reduction in the anisotropy field. This has a great effect on diminishing domain wall energy [15]. This result is in agreement of other published data [72]. Additionally, by annealing and increasing the particle size, H_c decreased slightly. In the present case, the magnetization mechanism occurred by domain wall motion because the particles are already in a multi-domain state and have larger domains by further annealing. This, in turn, reduces the number of domain walls [1]. The role of the domain wall energy is essentially to hinder the material from demagnetizing and consequently increase coercivity. But reducing the number of domain walls allows the material to demagnetize easily, hence reducing H_c [73]. Therefore, the material in this situation, with nearly zero H_c, is regarded as superparamagnetic instead of ferri-magnetic. In addition, the almost negligible coercive force permits easy magnetization and demagnetization with little magnetic loss [74]. Therefore, these materials may be considered good candidates for drug delivery and contrast agents in magnetic resonance imaging [31]. Hysteresis loop squareness values in all samples are relatively tiny, which implies that the samples have a set of randomly oriented domains. This is important in magnetic fluids [75].

Furthermore, the magnetic anisotropy field is required to specify the energy needed to change the magnetization direction from the easy direction to the magnetic field direction. It depends strongly on particle size, saturation magnetization, and coercivity [76]. Therefore, the magneto-crystalline anisotropy constant, K_1, is an important parameter and was calculated using Brown's relation $K_1 = \mu_0 \frac{M_s H_c}{0.96}$ [75], where $\mu_0 = 1$ in the CGS system. It is seen that K_1 decreases with increasing Cr^{3+} ions as a result of decreasing M_s and H_c, as listed in Table 8. In addition, K_1 depends on the particle size, as it decreases as the particle size decreases. This is because the surface-to-volume ratio increases, and the surface anisotropy contributes more than the bulk anisotropy. Surface atoms are known to have a different atomic configuration from bulk atoms. The spin-orbit coupling that causes the anisotropy effect varies significantly at the surface. These surface effects may result in lowering the overall magnetic anisotropy because surface atoms may not be as strongly aligned with the easy axes of the crystal as bulk atoms. Moreover, the effect of annealing on the anisotropy constant is obvious. It increases with annealing up to 900 °C because it enhances crystallinity by reducing defects such as voids and dislocations. The alignment of spins becomes easier and more ordered. However, K_1 increases by annealing at 1100 °C because of thermal agitation, which disrupts the alignment of magnetic moments by atomic diffusion or lattice vibrations [77].

3.7. Dielectric properties

The dielectric constant (ε'), ac conductivity (σ_{ac}), loss factor (tan δ), real part of impedance (Z'), and imaginary part (Z") of all

samples were found from the experimental data using the next equations [40,78]:

$$\varepsilon' = \frac{d}{\varepsilon_o A} C \tag{5}$$

$$\sigma_{ac} = 2\pi f \varepsilon_o \varepsilon' \tan \delta \tag{6}$$

$$\tan \delta = \frac{\varepsilon''}{\varepsilon'} \tag{7}$$

$$Z' = \frac{R}{1 + \omega^2 R^2 C^2} \tag{8}$$

$$Z'' = \frac{R\omega C}{1 + \omega^2 R^2 C^2} \tag{9}$$

where ε_o, d, and A are the permittivity of free space, the thickness of the samples, and the area of the pressed disc.

Fig. 9a and b shows the frequency dependence of the real part of the dielectric permittivity, ε', at room temperature for $Co_{0.7}Mn_{0.3}Cr_xFe_{x\text{-}2}O_4$ (x = 0.0, 0.6, 1.0) as-synthesized and annealed at 900 °C. Knowing that these as-synthesized samples were characterized before [79]. The observed dielectric dispersion mechanism can be described in terms of well-conducting grains (G), which are separated by non-conducting grain boundaries (GB) in solid materials. When the electrons arrive at the non-conducting grain boundaries, they are unable to cross the resistive grain boundary. As a result, interfacial polarization is created at the grain boundaries, where there is a large charge density (electrons). The resistivity difference between G and GB drives the charge carriers' collection at boundaries. This generates space charge polarization. At higher frequencies, the space charges fail to follow the alternating field, and consequently, there is little chance that they will reach the grain boundary [80].

On the other hand, as can be seen from TEM images, the as-prepared samples have an infinitesimal average particle size compared to the samples annealed at 900 °C, which clarifies why their ε' is larger in the as-prepared samples. Samples with tiny particles have more grain boundaries and the electrons are collected at the highly resistive grain boundaries, which induces space charge polarization.

Generally, the substitution of Fe^{3+} ions with Cr^{3+} ions at B-sites changes the material's dielectric properties. Fe^{3+} ions contribute to space charge polarization at the grain boundaries, which is essential for dielectric behavior. When Cr^{3+} replaces Fe^{3+} at B-sites in the crystal lattice of spinel ferrite, it lowers the available number of Fe^{3+} ions and alters the overall dielectric behavior of the material [41]. Therefore, these results are in agreement with earlier publications [81].

Fig. 10a and b displays the ac conductivity, σ'_{ac}, plotted as a function of frequency for $Co_{0.7}Mn_{0.3}Cr_xFe_{x\text{-}2}O_4$ (x = 0.0, 0.6, 1.0) samples as prepared and annealed at 900 °C. The curves depict two different regions. The two regions are components combined in a total conductivity equation:

$$\text{Total conductivity} = \sigma_{dc} + \sigma_{ac} \tag{10}$$

The first part of this formula is dc conductivity, or σ_{dc}, which is less reliant on frequency and occurs in the low frequency range. It is produced by band conduction. The second part is a frequency-dependent component linked to electron hopping at the octahedral sites that is known as ac conductivity, or σ_{ac}. At higher frequencies, σ_{ac} has a gradual exponential increase with increasing logarithmic frequency, obeying the power law [22]: $\sigma_{ac} = A\,\omega^s$.

It can therefore be concluded that a rise in the characteristic frequency is accompanied by an increase in conductivity. Considering this, the frequency corresponds to the reciprocal of the time. Alternatively, conductivity is enhanced with decreasing time. These results indicate that the time spent here is negligible compared to the ion's hopping duration [40]. The existence of transition metal elements with different valences is typically the primary source of hopping electrical conductivity in ferrites [22].

Increasing Cr^{3+} substitution significantly lowers the number of Fe^{3+} ions responsible for the hopping transition, resulting in a decrease in σ_{ac}. These dopants (Cr^{3+}) have no contribution to the conduct current but diminish the degree of electron transition between Fe^{2+} and Fe^{3+}.

It is important to note that the obvious increase in grain size with increasing annealing causes an increase in conductivity. This occurs because of reducing the number of grain boundaries, which prohibit electrons from passing among sites. An additional explanation for this rise in σ_{ac} is the greater probability of producing Fe^{2+} ions because of annealing. This improves the possibility of electron hopping between divalent and trivalent Fe ions, thereby improving conductivity.

On the other hand, the loss tangent, tan δ, expresses the energy loss within ferrite nanoparticles.

Fig. 11a and b displays that, with increasing the Cr^{3+} concentration, the dielectric loss, tan δ, decreases, as expected because of decreasing the dielectric constant. In addition, tan δ decreases by annealing, following the same behavior as ε'. Generally, the dielectric loss of a material is a result of a delay in polarization in the presence of the applied electric field. Grain boundaries, which are more effective in the low-frequency range, cause high resistivity and result in large dielectric loss at low frequencies (10^2–10^4 Hz). Due to the low resistive grains, there is a reduction in the loss tangent at high frequencies (10^5–10^6 Hz). Because less energy is required for electron exchange in the low-resistive grain layer, there is a reduction in loss. Therefore, low-dielectric-loss materials can be used as a potential candidate in communication devices [61].

Fig. 12a and b, and Fig. 13a and b illustrate how the real, Z′, and imaginary, Z″, components of impedance vary with frequency for

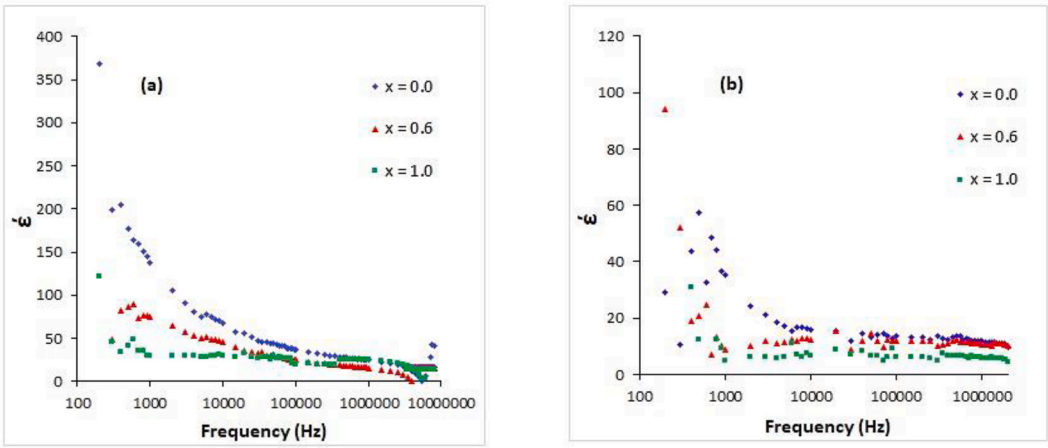

Fig. 9. The dielectric constant, e', as a function of frequency at room temperatures of Co0.7Mn0.3CrxFex-2O4 (x = 0.0, 0.6, 1.0) (a) as prepared (b) annealed at 900 °C.

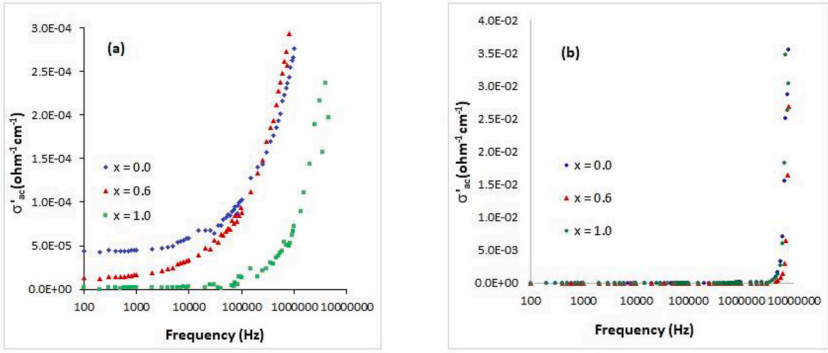

Fig. 10. The AC conductivity, s' ac, as a function of frequency at room temperatures of Co0.7Mn0.3CrxFex-2O4 (x = 0.0, 0.6, 1.0) (a) as prepared (b) annealed at 900 °C.

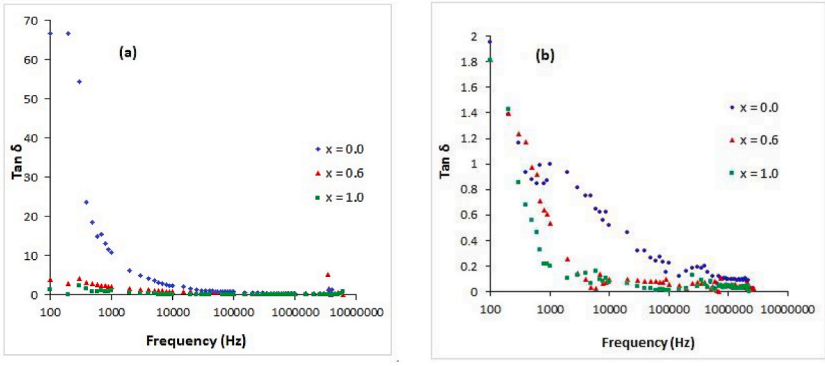

Fig. 11. The dielectric loss factor, Tan d, as a function of frequency at room temperatures of Co0.7Mn0.3CrxFex-2O4 (x = 0.0, 0.6, 1.0) (a) as prepared (b) annealed at 900 °C.

the as-prepared samples and samples annealed at 900 °C, respectively. The plot manifests that, for all samples, Z′ has an extremely high value at low frequency and drops thereafter. Z' is high in the low frequency range because of the influence of the high resistive grain boundary. While, in the high frequency region, the obvious frequency-independent behavior of Z′ is associated with a reduction in the effect of barrier existence and the release of the space charge [82]. It is important to mention that the lower value of Z′ indicates a higher conductivity [21].

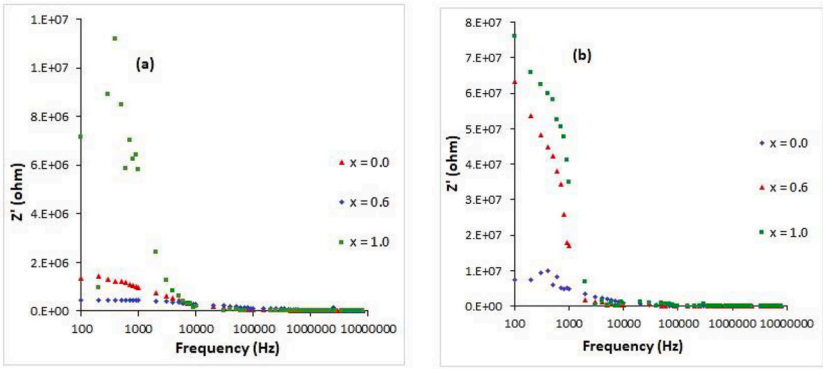

Fig. 12. The real part of impedance, Z′, as a function of frequency at room temperatures of Co0.7Mn0.3CrxFex2O4 (x = 0.0, 0.6, 1.0) (a) as prepared (b) annealed at 900 °C.

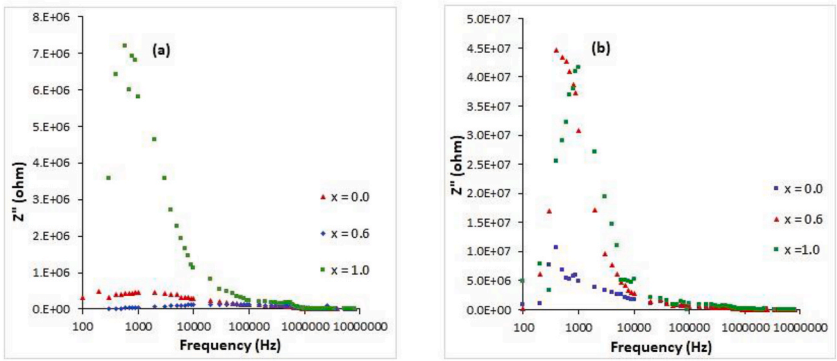

Fig. 13. The imaginary part of impedance, Z″, as a function of frequency at room temperatures of Co0.7Mn0.3CrxFex-2O4 (x = 0.0, 0.6, 1.0) (a) as prepared (b) annealed at 900 °C.

Z″, on the other hand, rises to a maximum value and then falls as frequency increases. The appearance of this broad peak is related to the relaxation phenomena that occur in the examined materials. The characteristic relaxation frequency (f_{max}) shifts toward the lower-frequency region as the chromium content increases because of a decrease in the hopping rate resulting from the reduction in conductivity. This outcome is consistent with the idea that raising the concentration of Cr ions reduces conductivity [80]. The peaks' intensity increased at the same time, and their width got narrower as the chromium content increased. The presence of lower intensive and broad peaks at low Cr^{3+} concentrations can be attributed to the existence of impurities. Whereas, the higher intensive and narrow peaks at low Cr^{3+} concentrations are explained by the inclusion of electrons [82].

The values of Z' and Z'' are found to be relatively high for the annealed samples compared to the as-prepared samples at low

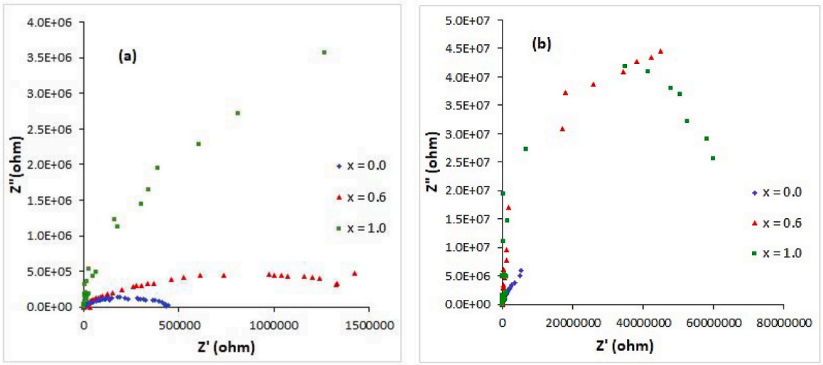

Fig. 14. The Nyquist (Cole-Cole) diagram, as a function of frequency at room temperatures, of Co0.7Mn0.3CrxFex-2O4 (x = 0.0, 0.6, 1.0) (a) as prepared (b) annealed at 900 °C.

frequencies. The impedance curves of the investigated materials interfere at high frequencies, which suggests the predominant contribution of low-resistive grains.

Fig. 14a and b displays the Nyquist diagram (Cole-Cole Z′ vs. Z″) for $Co_{0.7}Mn_{0.3}Cr_xFe_{2-x}O_4$ (x = 0, 0.6, 1) as-prepared and annealed at 900 °C. The Nyquist diagram displays two semicircular arcs. The first semicircle corresponds to the contribution of the grain boundary (GB) at lower frequencies, while the second semicircle is associated with the contribution of the grain (G) at higher frequencies. The difference in the semicircle diameter is indicative of a shift in the internal ohmic resistance of the sample's GB and G, which emerges as heat dissipation [83]. The only semicircular arc that is plainly visible is the GB one, and a parallel resistor-capacitor (RC) is its analogous circuit. The grain semicircle is extremely tiny and difficult to be seen in the graph, but parallel RC is also its equivalent circuit. The diameter of the GB semicircle varies because of changes in the ohmic resistance of the grain boundary.

4. Conclusion

The authors successfully synthesized $Co_{0.7}Mn_{0.3}Cr_xFe_{2-x}O_4$ nanoparticles via the co-precipitation technique, exhibiting its advantage in producing uniform particles within a limited size range. Despite exposure to high-temperature heating treatment, $Co_{0.7}Mn_{0.3}Cr_xFe_{2-x}O_4$ kept a very small average nanoscale particle size, as confirmed by both XRD and TEM analysis. The obtained $Co_{0.7}Mn_{0.3}Cr_xFe_{2-x}O_4$ has a narrow particle size distribution and a small standard deviation. These features are required in various fields such as drug delivery, catalysis, and materials science because they offer facilities for the exact and predictable performance of the nanoparticles in their promising applications. This leads to lowering the variations in ferrite nanoparticles' characteristics resulting from the variation in the size of the particles. This makes these materials more effective. Samples with higher Cr^{3+} content exhibited a near-zero coercive field and easy demagnetization, indicating compatibility for low magnetic loss applications. Being superparamagnetic, it is suggested that these materials can be used in engineering applications like transformers, motors, and ferrofluid, as well as medical applications including drug delivery and magnetic resonance imaging. Furthermore, the observed small dielectric constant values suggest suitability for high-frequency switching applications. In impedance analysis, the grain boundaries are known to control the conduction mechanism. In addition, the present samples have low dielectric loss. This makes these materials potential candidates for communication devices. Generally, this study indicates the multifunctionality of these co-precipitated ferrite nanoparticles in various technological applications.

Future work should be performed to enhance the properties of $Co_{0.7}Mn_{0.3}Cr_xFe_{2-x}O_4$. To investigate the elemental structural analysis of a material, X-ray photoelectron spectroscopy (XPS) will be done. Moreover, low-temperature vibrating sample magnetometry (VSM) and Mössbauer analysis will be used for an intensive study of the magnetic properties of $Co_{0.7}Mn_{0.3}Cr_xFe_{2-x}O_4$ nanoparticles. Additionally, it is significant to study the properties of these materials subjected to microwave radiation. This is because these samples can be used in radar and telecommunications systems.

Data and code availability

Not applicable.

CRediT authorship contribution statement

A.M. Elbashir: Funding acquisition. **M.M. Seada:** Data curation, Writing – original draft. **T.M. Meaz:** Conceptualization, Supervision. **E.H. El-Ghazzawy:** Writing – review & editing, Methodology, Data curation.

Declaration of competing interest

The authors declare that they have no known competing financial interests or personal relationships that could have appeared to influence the work reported in this paper.

Acknowledgement

The authors extend their appreciation to Prince Sattam bin Abdulaziz University for funding this research work through the project number (PSUA/2023/01/25671).

References

[1] A. Lassoued, J.F. Li, Structure and optical, magnetic and photocatalytic properties of Cr3+ substituted zinc nano-ferrites, J. Mol. Struct. 1262 (2022), https://doi.org/10.1016/j.molstruc.2022.133021.

[2] Z. Li, H. Jin, H. Wang, C. Wu, Q. Li, H. Dou, X. Jiang, Microstructure , magnetic properties , and loss performance of the Cu-substituted MnZn ferrites, Ceram. Int. 49 (2023) 40275–40283, https://doi.org/10.1016/j.ceramint.2023.09.363.

[3] B. Trinadh, J. Suresh, G.R. Patta, K.V. Babu, C. Komali, B.V. Babu, K.A. Devi, B.S. Mohan, K. Samatha, Structural , optical , electrical and magnetic properties of aluminum substituted Co – Cu – Zn nano-crystalline ferrites, Solid State Commun. 376 (2023) 115360, https://doi.org/10.1016/j.ssc.2023.115360.

[4] K. Kaur, T. Tekou, C. Trudel, K. Rani, A.K. Srivastava, D. Basandrai, Crystal structure refinement, morphological, and magnetic properties of ternary nanohybrid Prx Mn0.5Co0.5 Fe2−xO.4 (0 . 0 < x < 0 . 04) spinel ferrite, Inorg. Chem. Commun. 159 (2024) 111717, https://doi.org/10.1016/j.inoche.2023.111717.

[5] B. Rezaei, A. Kermanpur, S. Labbaf, Effect of Mn addition on the structural and magnetic properties of Zn-ferrite nanoparticles, J. Magn. Magn Mater. 481 (2019) 16–24, https://doi.org/10.1016/j.jmmm.2019.02.085.

[6] M.G. Moustafa, H.H. Hamdeh, M.A. Sebak, M.H. Mahmoud, Mö ssbauer spectral analysis and magnetic properties of the superparamagnetic Mn0.5Zn0.5Fe2O4 ferrite nanocomposites, Mater. Today Commun. 37 (2023) 107090, https://doi.org/10.1016/j.mtcomm.2023.107090.

[7] T. Dippong, E.A. Levei, C. Leostean, O. Cadar, Impact of annealing temperature and ferrite content embedded in SiO2 matrix on the structure, morphology and magnetic characteristics of (Co0.4Mn0.6Fe2O4)δ (SiO2)100-δ nanocomposites, J. Alloys Compd. 868 (2021) 159203, https://doi.org/10.1016/j.jallcom.2021.159203.

[8] M. Stoia, M. Stefanescu, T. Dippong, O. Stefanescu, P. Barvinschi, Low temperature synthesis of Co2SiO4/SiO2 nanocomposite using a modified sol-gel method, J. Sol. Gel Sci. Technol. 54 (2010) 49–56, https://doi.org/10.1007/s10971-010-2156-2.

[9] M. Ştefănescu, T. Dippong, M. Stoia, O. Ştefănescu, Study on the obtaining of cobalt oxides by thermal decomposition of some complex combinations, undispersed and dispersed in SiO 2 matrix, J. Therm. Anal. Calorim. 94 (2008) 389–393, https://doi.org/10.1007/s10973-008-9111-2.

[10] N. Bentarhlia, M. Elansary, M. Belaiche, Y. Mouhib, O.M. Lemine, H. Zaher, Evaluating of novel Mn – Mg – Co ferrite nanoparticles for biomedical applications : from synthesis to biological activities, Ceram. Int. 49 (2023) 40421–40434, https://doi.org/10.1016/j.ceramint.2023.10.017.

[11] T. Dippong, E.A. Levei, F. Goga, O. Cadar, Influence of Mn2+ substitution with Co2+ on structural, morphological and coloristic properties of MnFe2O4/SiO2 nanocomposites, Mater. Char. 172 (2021) 110835, https://doi.org/10.1016/j.matchar.2020.110835.

[12] F. Hcini, S. Hcini, B. Alzahrani, S. Zemni, M.L. Bouazizi, Effect of Cr substitution on structural, magnetic and impedance spectroscopic properties of Cd0.5Zn0.5Fe2−xCrxO4 ferrites, Appl. Phys. Mater. Sci. Process 126 (2020) 1–14, https://doi.org/10.1007/s00339-020-03544-z.

[13] K.P.S. Phadke, M.D.A. Mishra, Synthesis and characterization of Cr substituted Mn – Zn nanoferrites with improved dielectric , electrical conductivity and impedance properties for electronic device applications, J. Korean Ceram. Soc. 59 (2022) 427–435, https://doi.org/10.1007/s43207-022-00197-x.

[14] S. Ouyahia, A. Rais, B. Bozzo, K. Taibi, A. Addou, Cations distribution by Rietveld refinement and magnetic properties of MgCrxFe2−xO4 spinel ferrites, Appl. Phys. Mater. Sci. Process 126 (2020) 1–9, https://doi.org/10.1007/s00339-020-03865-z.

[15] B. Dey, M. Bououdina, G. Abd, P. Dhamodharan, S. Asathbahadur, M. Venkateshwarlu, C. Manoharan, Tuning the gas sensing properties of spinel ferrite NiFe2O4 nanoparticles by Cu doping, J. Alloys Compd. 970 (2024) 172711, https://doi.org/10.1016/j.jallcom.2023.172711.

[16] T. Dippong, D. Toloman, M. Dan, E.A. Levei, O. Cadar, Structural, morphological and photocatalytic properties of Ni-Mn ferrites: influence of the Ni:Mn ratio, J. Alloys Compd. 913 (2022) 1–9, https://doi.org/10.1016/j.jallcom.2022.165129.

[17] T. Dippong, E.A. Levei, D. Toloman, L. Barbu-Tudoran, O. Cadar, Investigation on the formation, structural and photocatalytic properties of mixed Mn-Zn ferrites nanoparticles embedded in SiO2 matrix, J. Anal. Appl. Pyrolysis 158 (2021) 105281, https://doi.org/10.1016/j.jaap.2021.105281.

[18] S. Arsalani, Y. Hadadian, E.E. Mazon, E.J. Guidelli, E. Kava, A.P. Ramos, A.J. Gualdi, T.Z. Pavan, O. Baffa, A.A.O. Carneiro, Uniform size PEGylated iron oxide nanoparticles as a potential theranostic agent synthesized by a simple optimized coprecipitation route, J. Magn. Magn Mater. 564 (2022) 170091, https://doi.org/10.1016/j.jmmm.2022.170091.

[19] C. Srinivas, B.V. Tirupanyam, S.S. Meena, S.M. Yusuf, C.S. Babu, K.S. Ramakrishna, D.M. Potukuchi, D.L. Sastry, Structural and magnetic characterization of co-precipitated NixZn1-xFe2O4 ferrite nanoparticles, J. Magn. Magn Mater. 407 (2016) 135–141, https://doi.org/10.1016/j.jmmm.2016.01.060.

[20] A.A. Ibiyemi, O. Akinrinola, G.T. Yusuf, Photoelectric and optoelectronic effects of hard ferromagnetic manganese cobalt (Mn–Co) ferrite nanoparticles for high-frequency device application, Appl. Phys. Mater. Sci. Process 128 (2022) 1–18, https://doi.org/10.1007/s00339-022-05926-x.

[21] M. Horchani, A. Omri, M.S. Eddine, A. Benali, A. Tozri, E. Dhahri, K. Pavani, B.F.O. Costa, M.F.P. Graca, Ni–Cu–Co ferrite synthesized using the sol–gel method: effects of the Cr3+ ion concentration on its structural, electrical, and dielectric properties, Appl. Phys. Mater. Sci. Process 128 (2022) 1–16, https://doi.org/10.1007/s00339-022-06053-3.

[22] M.H. Nasr, M.M. Elkholy, L.M.S. El-Deen, A.S. Abouhaswa, G.M. Turky, A.A. El-Hamalawy, A comprehensive study on crystal structure, magnetic, and electrical properties of Ni-doped Fe–Cd spinel nano-ferrites, J. Mater. Sci. Mater. Electron. 33 (2022) 15652–15664, https://doi.org/10.1007/s10854-022-08469-2.

[23] G. Lal, K. Punia, S.N. Dolia, P.A. Alvi, B.L. Choudhary, S. Kumar, Structural, cation distribution, optical and magnetic properties of quaternary Co0.4+xZn0.6-xFe2O4 (x = 0.0, 0.1 and 0.2) and Li doped quinary Co0.4+xZn0.5-xLi0, J. Alloys Compd. 828 (2020), https://doi.org/10.1016/j.jallcom.2020.154388, 1Fe2O4 (x = 0.0, 0.05 and 0.1) nanoferrites.

[24] R. Ranga, K. Kumar, A. Kumar, Influence of Ce3+ ion doping on structural , morphological , magnetic , ferrite nanoparticles synthesized via coprecipitation method, J. Magn. Magn Mater. 588 (2023) 171496, https://doi.org/10.1016/j.jmmm.2023.171496.

[25] S. ullah Rather, H.S. Bamufleh, H. Alhumade, A.A. Taimoor, U. Saeed, A.A. Al-Zahrani, O.M. Lemine, Morphological, structural, surface, thermal, chemical, and magnetic properties of Al-doped nanostructured copper ferrites, Ceram. Int. 49 (2023) 20261–20272, https://doi.org/10.1016/j.ceramint.2023.03.149.

[26] B.L. Choudhary, U. Kumar, S. Kumar, S. Chander, S. Kumar, S. Dalela, S.N. Dolia, P.A. Alvi, Irreversible magnetic behavior with temperature variation of Ni0.5Co0.5Fe2O4 nanoparticles, J. Magn. Magn Mater. 507 (2020) 166861, https://doi.org/10.1016/j.jmmm.2020.166861.

[27] G. Magesh, G. Bhoopathi, A.P. Arun, E. Ranjith Kumar, C. Srinivas, S. Sathiyaraj, Study of structural, morphological, optical and biomedical properties of pH based ZnO nanostructures, Superlattice. Microst. 124 (2018) 41–51, https://doi.org/10.1016/j.spmi.2018.10.002.

[28] H. Ghorbani, Study on the effects of cadmium and chromium substitution in hydrothermally-synthesized spinel cobalt ferrite nanoparticles, Eur. Phys. J. Plus 822 (2023) 1–12, https://doi.org/10.1140/epjp/s13360-023-04436-w.

[29] C. Srinivas, B.V. Tirupanyam, A. Satish, V. Seshubai, D.L. Sastry, O.F. Caltun, Effect of Ni2+ substitution on structural and magnetic properties of Ni-Zn ferrite nanoparticles, J. Magn. Magn Mater. 382 (2015) 15–19, https://doi.org/10.1016/j.jmmm.2015.01.008.

[30] C. Srinivas, E. Ranjith Kumar, B.V. Tirupanyam, S. Singh Meena, P. Bhatt, C.L. Prajapat, T.V. Chandrasekhar Rao, D.L. Sastry, Study of magnetic behavior in co-precipitated Ni–Zn ferrite nanoparticles and their potential use for gas sensor applications, J. Magn. Magn Mater. 502 (2020) 166534, https://doi.org/10.1016/j.jmmm.2020.166534.

[31] O. Karaagac, H. Köçkar, Improvement of the saturation magnetization of PEG coated superparamagnetic iron oxide nanoparticles, J. Magn. Magn Mater. 551 (2022) 169140, https://doi.org/10.1016/j.jmmm.2022.169140.

[32] M.L. Bouazizi, S. Hcini, K. Khirouni, M.H. Dhaou, F. Najar, A.H. Alshehri, Annealing temperature effects on structural, magnetic, and optoelectronic properties of mixed Ni0.6Mg0.2Co0.2FeCrO4 ferrites, J. Electron. Mater. 52 (2023) 2878–2893, https://doi.org/10.1007/s11664-023-10254-8.

[33] A. Hossain, A.R. Gilev, P. Yanda, V.A. Cherepanov, A.S. Volegov, K. Sakthipandi, A. Sundaresan, Optical, magnetic and magneto-transport properties of Nd 1-xAxMn0.5Fe0.5O3-δ (A=Ca, Sr, Ba; x=0, 0.25), J. Alloys Compd. 847 (2020) 1–9, https://doi.org/10.1016/j.jallcom.2020.156297.

[34] N.R. Rethi, J. Johnson, A. Murugeswari, R. Sankaranarayanan, Role of Al3+ and Ti4+ ions on structural, optical and electrical properties of AlyTixZn(0.4−y)Ni(0.6−x)Fe2O4 nanoparticles, J. Mater. Sci. Mater. Electron. 34 (2023) 1–16, https://doi.org/10.1007/s10854-023-10244-w.

[35] H. Ghorbani, M. Eshraghi, A.A.S. Dodaran, Structural and magnetic properties of cobalt ferrite nanoparticles doped with cadmium, Phys. B Phys. Condens. Matter 634 (2022) 413816, https://doi.org/10.1016/j.physb.2022.413816.

[36] C. Srinivas, M. Deepty, E.R. Kumar, S.A.V. Prasad, B.V. Tirupanyam, S.S. Meena, C.L. Prajapat, D.L. Sastry, Rietveld refinement and FTIR spectroscopic studies of Ni2+-substituted Zn-ferrite nanoparticles, Appl. Phys. Mater. Sci. Process 125 (2019) 1–10, https://doi.org/10.1007/s00339-019-2840-1.

[37] S. Hasan, B. Azhdar, Effect of annealing temperature, annealing time, and hydrogen potential on the physical properties of Ni0.5Zn0.5Fe2O4 nanoparticles, Ceram. Int. 49 (2023) 5371–5381, https://doi.org/10.1016/j.ceramint.2022.10.060.

[38] K.G. Saija, N.H. Vasoya, S.K. Modi, U.M. Meshiya, K.K. Jani, P.Y. Raval, K.B. Modi, Bulk magnetization, temperature - dependent ac susceptibility and dc resistivity study on Mn0.7+xZn0.3SixFe2-2xO4 (x = 0.0–0.3) spinel ferrites, Phys. B Condens. Matter 593 (2020) 412302, https://doi.org/10.1016/j.physb.2020.412302.

[39] A. Gaffoor, K.C.B. Naidu, D. Ravinder, K.M. Batoo, S.F. Adil, M. Khan, Synthesis of nano-NiXFe2O4 (X = Mg/Co) by citrate-gel method: structural, morphological and low-temperature magnetic properties, Appl. Phys. Mater. Sci. Process 126 (2020) 1–20, https://doi.org/10.1007/s00339-019-3225-1.

[40] R. Verma, P. Thakur, A.C. Aidan Sun, A. Thakur, Investigation of structural, microstructural and electrical characteristics of hydrothermally synthesized Li0.5-0.5xCoxFe2.5-0.5xO4, (0.0 ≤ x≤ 0.4) ferrite nanoparticles, Phys. B Condens. Matter 661 (2023) 414926, https://doi.org/10.1016/j.physb.2023.414926.

[41] M.M. Rahman, N. Hasan, M.A. Hoque, M.B. Hossen, M. Arifuzzaman, Structural, dielectric, and electrical transport properties of Al3+ substituted nanocrystalline Ni-Cu spinel ferrites prepared through the sol–gel route, Results Phys. 38 (2022) 105610, https://doi.org/10.1016/j.rinp.2022.105610.

[42] N. Suo, A. Sun, Y. Zhang, L. Yu, L. Shao, Z. Zuo, Magnetic transformation of Ni–Mg–Zn ferrite substituted by the Co2+ ions from soft magnetic to hard magnetic, J. Mater. Sci. Mater. Electron. 32 (2021) 3286–3302, https://doi.org/10.1007/s10854-020-05077-w.

[43] A.E. Elkholy, F. El-Taib Heakal, N.K. Allam, Nanostructured spinel manganese cobalt ferrite for high-performance supercapacitors, RSC Adv. 7 (2017) 51888–51895, https://doi.org/10.1039/c7ra11020k.

[44] N.I. Abu-Elsaad, A.S. Nawara, S.A. Mazen, Synthesis, structural characterization, and magnetic properties of Ni–Zn nanoferrites substituted with different metal ions (Mn2+, Co2+, and Cu2+), J. Phys. Chem. Solid. 146 (2020) 109620, https://doi.org/10.1016/j.jpcs.2020.109620.

[45] R.R. Kanna, K. Sakthipandi, A.S. Kumar, N.R. Dhineshbabu, S.M.S.M.A. Maraikkayar, A.S. Afroze, R.B. Jotania, M. Sivabharathy, Synthesis of dysprosium/Mn–Cu ferrite binary nanocomposite: analysis of structural, morphological, dielectric, and optomagnetic properties, Ceram. Int. 46 (2020) 13695–13703, https://doi.org/10.1016/j.ceramint.2020.02.157.

[46] H. Malik, M.A. Khan, M.N. Akhtar, S. Gulbadan, S.R. Ejaz, Tailoring of structural, dielectric, and magnetic properties of SrBaCu2Fe12O22 hexaferrites by doping with Gd–Co binary mixtures, Appl. Phys. Mater. Sci. Process 128 (2022) 1–11, https://doi.org/10.1007/s00339-022-05861-x.

[47] S. Kumar, P.B. Barman, R. Raj Singh, Estimation and association of structural, elastic and magnetic properties of magnesium-nickel-ferrite nanoparticles annealed at different temperatures, Mater. Sci. Eng. B 272 (2021) 115362, https://doi.org/10.1016/j.mseb.2021.115362.

[48] M.M. Hossen, S. Nasrin, M.B. Hossen, Effect of Mn2+ doping on structural , magnetic and electrical properties of combustion method for high-frequency applications, Phys. B Phys. Condens. Matter 599 (2020) 412456, https://doi.org/10.1016/j.physb.2020.412456.

[49] S. Jesus Mercy, N. Murali, A. Ramakrishna, Y. Ramakrishna, V. Veeraiah, K. Samatha, Microstructural, thermal, electrical and magnetic analysis of Mg2+ substituted Cobalt ferrite, Appl. Phys. Mater. Sci. Process 126 (2020) 1–13, https://doi.org/10.1007/s00339-020-04048-6.

[50] M.A. Gabal, E. Al-Mutairi, Y.M. Al Angari, A. Awad, A.A. Al-Juaid, A. Saeed, Synthesis, characterization, elastic, and electro-magnetic properties of MFe2O4 ferrites (M = Co2+, Ni2+, Cu2+, Mg2+, and Zn2+) via sucrose auto-combustion, J. Mater. Res. 37 (2022) 2257–2270, https://doi.org/10.1557/s43578-022-00624-z.

[51] M.S. Hasan, S.S. Ali, M. Rizwan, M.I. Khan, H.M. Naeem Ullah, M.I. Irfan, Structural, optical, electrical and magnetic properties of Cu0.2Zn0.2Ni0.6-xMgxFe2O4 (x = 0.00, 0.15, 0.30, 0.45, 0.60) soft ferrites, J. Alloys Compd. 956 (2023), https://doi.org/10.1016/j.jallcom.2023.170392.

[52] S.E. Mousavi Ghahfarokhi, E.M. Shobegar, M.Z. Shoushtari, Effects of sintering temperature on structural, morphological and magnetic properties of strontium ferrite nanoparticles, J. Supercond. Nov. Magnetism 32 (2019) 1067–1076, https://doi.org/10.1142/S0217984918503219.

[53] E.H. El-Ghazzawy, Effect of heat treatment on structural, magnetic, elastic and optical properties of the co-precipitated Co0.4Sr0.6Fe2O4, J. Magn. Magn Mater. 497 (2020) 166017, https://doi.org/10.1016/j.jmmm.2019.166017.

[54] A.S. Abouhaswa, M.H. Badr, M.H. Nasr, M.M. Elkholy, L.M.S. El-Deen, G.M. Turky, M. Moustafa, A.A. El-Hamalawy, Investigation of crystal structure, electrical and magnetic properties of spinel Mn-Cd ferrite nanoparticles, J. Inorg. Organomet. Polym. Mater. 32 (2022) 486–498, https://doi.org/10.1007/s10904-021-02116-9.

[55] G. Lal, K. Punia, H. Bhoi, S.N. Dolia, B.L. Choudhary, P.A. Alvi, S. Dalela, S.K. Barbar, S. Kumar, Exploring the structural, elastic, optical, dielectric and magnetic characteristics of Ca2+ incorporated superparamagnetic Zn0.5−xCa0.1Co0, 4+xFe2O4 (x = 0.0, 0.05 & 0.1) nanoferrites, J. Alloys Compd. 886 (2021) 161190, https://doi.org/10.1016/j.jallcom.2021.161190.

[56] E.H. El-Ghazzawy, H.M.H. Zakaly, A.W. Alrowaily, S.A. Saafan, A. Ene, N.M. Abo-aita, M.A. Darwish, D. Zhou, A.S. Atlam, Delving into the properties of nanostructured Mg ferrite and PEG composites: a comparative study on structure, electrical conductivity, and dielectric relaxation, Heliyon 9 (2023) e19745, https://doi.org/10.1016/j.heliyon.2023.e19745.

[57] R. Singh Yadav, I. Kuřitka, J. Havlica, M. Hnatko, C. Alexander, J. Masilko, L. Kalina, M. Hajdúchová, J. Rusnak, V. Enev, Structural, magnetic, elastic, dielectric and electrical properties of hot-press sintered Co1−xZnxFe2O4 (x = 0.0, 0.5) spinel ferrite nanoparticles, J. Magn. Magn Mater. 447 (2018) 48–57, https://doi.org/10.1016/j.jmmm.2017.09.033.

[58] S.E.M. Ghahfarokhi, E.M. Shobegar, M.Z. Shoushtari, Preparation and characterization of spinel SrFe2O4 nanoparticles by method sol-gel, J. Australas. Ceram. Soc. 57 (2021) 1359–1369, https://doi.org/10.1007/s41779-021-00633-x.

[59] P. Monisha, P. Priyadharshini, S.S. Gomathi, K. Pushpanathan, Influence of Mn dopant on the crystallite size, optical and magnetic behaviour of CoFe2O4 magnetic nanoparticles, J. Phys. Chem. Solid. 148 (2021) 109654, https://doi.org/10.1016/j.jpcs.2020.109654.

[60] K. Sakthipandi, K. Kannagi, A. Hossain, Effect of lanthanum doping on the structural, electrical, and magnetic properties of Mn0.5Cu0.5LaxFe2−xO4 nanoferrites, Ceram. Int. 46 (2020) 19634–19638, https://doi.org/10.1016/j.ceramint.2020.04.255.

[61] B. Mishra, B. Munisha, J. Nanda, K.J. Sankaran, S. Suman, Hydrothermally Synthesized Magnesium doped Zinc Ferrite Nanoparticles: an extensive study on structural, optical, magnetic, and dielectric properties, Mater. Chem. Phys. 292 (2022) 126791, https://doi.org/10.1016/j.matchemphys.2022.126791.

[62] C.N. Potangale, S.K. Pardeshi, Effect of Ni2+ substitution on magnetic, optical and electrical properties of SrFe2O4, Mater. Sci. Eng. B 283 (2022) 115848, https://doi.org/10.1016/j.mseb.2022.115848.

[63] B. Gayathri Manju, P. Raji, Green synthesis, characterization, and antibacterial activity of lime-juice-mediated copper–nickel mixed ferrite nanoparticles, Appl. Phys. Mater. Sci. Process 126 (2020) 1–12, https://doi.org/10.1007/s00339-020-3313-2.

[64] A. Ur Rehman, G. Abbas, B. Ayoub, N. Amin, M. Ajaz un Nabi, N.A. Morley, M. Akhtar, M. Imran Arshad, M. Uzair Khalid, M. Afzaal, A. Ghuffar, M. Arshad, Impact of Ni2+ on the structural, optical, electrical, and dielectric properties of Cu0.25Co0.25Mg0.5-xNixCe0.03Fe1.97O4 spinel ferrites synthesized via sol-gel auto combustion (SGAC) route, Mater. Sci. Eng. B Solid-State Mater. Adv. Technol. 291 (2023), https://doi.org/10.1016/j.mseb.2023.116407.

[65] V. Tukaram, S.S. Shinde, R.B. Borade, A.B. Kadam, Study of cation distribution, structural and electrical properties of Al–Zn substituted Ni–Co ferrite, Phys. B Condens. Matter 577 (2020) 411783, https://doi.org/10.1016/j.physb.2019.411783.

[66] R. Samad, M. ud D. Rather, K. Asokan, B. Want, Dielectric and magnetic properties of rare-earth-doped cobalt ferrites and their first-order reversal curve analysis, Appl. Phys. Mater. Sci. Process 125 (2019) 1–12, https://doi.org/10.1007/s00339-019-2804-5.

[67] T. Dippong, E.A. Levei, I. Grigore Deac, P. I, G. Borodi, O. Cadar, Sol-gel synthesis, structure, morphology and magnetic properties of Ni0.6Mn0.4Fe2O4 nanoparticles embedded in SiO2 matrix thomas, Nanomater. Artic. 11 (2021) 1–15.

[68] M.A. Almessiere, Y. Slimani, A. Baykal, Structural and magnetic properties of Ce-doped strontium hexaferrite, Ceram. Int. 44 (2018) 9000–9008, https://doi.org/10.1016/j.ceramint.2018.02.101.

[69] S. Kaur, V. Kumar, R. Jasrotia, V. Bhasin, Spinel nanoferrite (CoFe 2 O 4): the impact of Cr doping on its structural , surface morphology , magnetic , and antibacterial activity traits Spinel nanoferrite (CoFe 2 O 4): the impact of Cr doping on its structural , surface morphology , magnetic, Opt. Mater. 133 (2022) 113026, https://doi.org/10.1016/j.optmat.2022.113026.

[70] K. Sakthipandi, B. Ganesh Babu, G. Rajkumar, A. Hossian, M. Srinidhi Raghavan, M. Rajesh Kumar, Investigation of magnetic phase transitions in Ni0.5Cu0.25Zn0.25Fe2-xLaxO4 nanoferrites using magnetic and in-situ ultrasonic measurements, Phys. B Condens. Matter 645 (2022) 414280, https://doi.org/10.1016/j.physb.2022.414280.

[71] H. Khedri, A. Gholizadeh, Experimental comparison of structural, magnetic and elastic properties of M0.3Cu0.2Zn0.5Fe2O4 (M = Cu, Mn, Fe, Co, Ni, Mg) nanoparticles, Appl. Phys. Mater. Sci. Process 125 (2019) 1–13, https://doi.org/10.1007/s00339-019-3010-1.

[72] R. Rajini, A. Christy Ferdinand, Effects of annealing on the structural, morphological and magnetic properties of CuFe2O4 Ferrite Nanoparticles synthesized by chemical precipitation, Chem. Data Collect. 44 (2023) 100985, https://doi.org/10.1016/j.cdc.2022.100985.

[73] B.L. Choudhary, N. Kumari, J. Kumari, A. Kumar, S.N. Dolia, Relaxation mechanism in Ni0.5Zn0.5Fe2O4 nanocrystalline ferrite at a lower temperature, Mater. Lett. 304 (2021) 130731, https://doi.org/10.1016/j.matlet.2021.130731.

[74] A. Hossain, P. Yanda, V.A. Cherepanov, K. Sakthipandi, A. Sundaresan, Synthesis, structure, optical and magnetic properties of Nd1−xAxMn0.5Co0.5O3−δ (A = Ba, Sr and Ca; x = 0 and 0.25), Ceram. Int. 46 (2020) 26895–26902, https://doi.org/10.1016/j.ceramint.2020.07.166.

[75] M. Zulqarnain, S.S. Ali, U. Hira, J.F. Feng, M.I. Khan, M. Rizwan, K. Javed, G. Farid, M.S. Hasan, Superparamagnetic contributions, optical band gap tuning and dominant interfacial resistive mechanisms in ferrites nanostructures, J. Alloys Compd. 894 (2022) 162431, https://doi.org/10.1016/j.jallcom.2021.162431.

[76] E.E. Ateia, A.T. Mohamed, M. Maged, A. Abdelazim, Crystal structures and magnetic properties of polyethylene glycol/polyacrylamide encapsulated CoCuFe4O8 ferrite nanoparticles, Appl. Phys. Mater. Sci. Process 126 (2020) 1–10, https://doi.org/10.1007/s00339-020-03841-7.

[77] M. Aliuzzaman, M. Manjurul Haque, M. Jannatul Ferdous, S. Manjura Hoque, M. Abdul Hakim, Effect of sintering time on the structural , magnetic and electrical transport properties of, Sci. Res. 2014 (2014) 13–23.
[78] A.M. El-naggar, Z.K. Heiba, A.M. Kamal, M.B. Mohamed, The role of cobalt amount in ZnCdS nanofiller on the optical, thermal, dielectric and structure properties of PVA/PVP/PEG blends, Opt. Quant. Electron. 55 (2023) 1–18, https://doi.org/10.1007/s11082-023-04886-7.
[79] T.M. Meaz, M.M. Seada, Controlling the structural and physical properties of as-synthesized Co-Mn ferrite nanoparticles by adding Cr ions, Egypt, J. Solids 42 (2020) 1–20, https://doi.org/10.21608/ejs.2020.147994.
[80] S. Matteppanavar Hanamanta, B.G. Hegde, Magnetic and electrical investigations of low dimensional Co0.5Zn0.5−xCuxFe2O4 nano ferrites, J. Alloys Compd. 954 (2023) 170031, https://doi.org/10.1016/j.jallcom.2023.170031.
[81] M. Mumtaz Mubasher, M. Hassan, L. Ali, Z. Ahmad, M.A. Imtiaz, M.F. Aamir, A. Rehman, K. Nadeem, Comparative study of frequency-dependent dielectric properties of ferrites MFe2O4 (M = Co, Mg, Cr and Mn) nanoparticles, Appl. Phys. Mater. Sci. Process 126 (2020) 1–14, https://doi.org/10.1007/s00339-020-03529-y.
[82] T. Şaşmaz Kuru, Synthesis and investigation of structural, dielectric, impedance, conductivity and humidity sensing properties of Cr3+-substituted Mg–Zn ferrite nanoparticle, Appl. Phys. Mater. Sci. Process 126 (2020) 1–10, https://doi.org/10.1007/s00339-020-03575-6.
[83] S.T. Assar, E.H. El-Ghazzawy, H.F. Abosheiasha, Study on dielectric properties, electric modulus, and impedance spectroscopy of Ni–Ca ferrite nanoparticles, Mater. Chem. Phys. 287 (2022) 126336, https://doi.org/10.1016/j.matchemphys.2022.126336.